



1 **Precambrian faulting episodes and insights into the tectonothermal history**
2 **of North Australia: Microstructural evidence and K–Ar, ^{40}Ar – ^{39}Ar , and**
3 **Rb–Sr dating of syntectonic illite from the intracratonic Millungera Basin.**

4 *I. Tonguç Uysal¹, Claudio Delle Piane¹, Andrew Todd¹ and Horst Zwingmann²*

5 ¹*CSIRO Energy, 26 Dick Perry Avenue, Kensington WA 6151, Australia*

6 ²*Department of Geology and Mineralogy, Kyoto University, Kitashirakawa Oiwake-cho,*
7 *Kyoto 606-8502, Japan.*

8 **ABSTRACT**

9 Australian terranes concealed beneath Mesozoic cover record complex Precambrian
10 tectonic histories involving a successive development of several Proterozoic to Paleozoic
11 orogenic systems. This study presents an integrated approach combining K–Ar, ^{40}Ar – ^{39}Ar ,
12 and Rb–Sr geochronology of Precambrian authigenic illites from the recently discovered
13 Millungera Basin in north-central Australia. Brittle deformation and repeated fault activity
14 are evident from the sampled cores and their microstructures, probably associated with the
15 large-scale faults inferred from interpretations of seismic survey. Rb–Sr isochron, ^{40}Ar – ^{39}Ar
16 total gas, and K–Ar ages are largely consistent indicating late Mesoproterozoic and early
17 Proterozoic episodes ($\sim 1115 \pm 26$ Ma, $\sim 1070 \pm 25$ Ma, $\sim 1040 \pm 24$ Ma, $\sim 1000 \pm 23$ Ma, and
18 $\sim 905 \pm 21$ Ma) of active tectonics in north-central Australia. K–Ar results show that illites
19 from fault gouges and authigenic matrix illites in undeformed adjacent sandstones
20 precipitated contemporaneously, indicating that advection of tectonically mobilised fluids
21 extended into the undeformed wall rocks above or below the fracture and shear (fault gouge)
22 zones. This study provides insight into the enigmatic time-space distribution of Precambrian



23 tectonic zones in central Australia, which are responsible for the formation of a number of
24 sedimentary basins with significant energy and mineral resources.

25 Keywords: Fault gouge; illite; micro structure; fluid flow; isotope dating; Precambrian;
26 Australia.

27 **1. INTRODUCTION**

28 Direct dating of brittle faulting is crucial for determining the absolute timing of
29 inscrutable time-space distribution of tectonothermal events in concealed Precambrian
30 terranes. Over the last decade, dating of illitic clay from near-surface fault gouges has
31 increasingly become a routine approach to defining the timing of brittle deformations (van
32 der Pluijm et al., 2001; Uysal et al., 2006; Mutlu et al., 2010; Zwingmann and Mancktelow,
33 2004, Zwingmann et al., 2010; Duvall et al., 2011; Hetzel et al., 2013, Torgersen et al., 2014;
34 Mancktelow et al., 2016, Viola et al., 2016; Babaahmadi et al., 2019). This technique has
35 been particularly useful in better understanding the development of convergent plate
36 boundaries and continental collisions (e.g., van der Pluijm et al., 2001; Duvall et al., 2011;
37 Isik et al., 2015; Babaahmadi et al. 2019), movements along transform plate margins (Uysal
38 et al., 2006; Mutlu et al., 2009; Boles et al., 2015), and the formation of orocline bending
39 accompanied by regional strike-slip faulting (Rosenbaum et al., 2015).

40 While fault gouges reported by earlier studies were mainly from surface outcrops,
41 dating of concealed fault systems is more challenging due to the lack of direct structural
42 observations. Although unknown fault systems buried under thick sedimentary basins can be
43 denoted by geophysical techniques such 2D and 3D seismic reflections, cores from boreholes
44 shaft or tunnel sites intersecting fault zones can be used to date fault reactivation episodes
45 (e.g., Viola et al., 2013; Yamasaki et al., 2013, Elminen et al., 2018). The current study
46 investigates fault rocks and the host sandstone intersected in drill cores from the newly



47 discovered Millungera Basin in north Queensland, north-central Australia (Fig. 1). It
48 demonstrates how illite geochronology in combination with microstructural and
49 mineralogical studies can be used to define a concealed, previously unrecorded Proterozoic
50 tectonic events. Prior to this study (Fig. 1), almost no geological information was available on
51 the Precambrian geology of large parts of north-central Australia, including the Millungera
52 Basin, except for some regional geophysical data (Korsch et al., 2011, 2012) (Fig. 1). This is
53 due to an extensive cover of sediments of the Jurassic–Cretaceous Eromanga-Carpentaria
54 Basin (Fig. 1). Further uncertainties in tectonic interpretation of Australian Precambrian
55 terranes arises from the tendency for original tectonic information to be masked by younger
56 tectonics. Therefore, a major objective of this study was to provide insight into the enigmatic
57 time-space distribution of Mid- to Late- Mesoproterozoic tectonic zones in central Australia,
58 which are responsible for the formation of a number of sedimentary basins with significant
59 potential for energy and mineral resources (Korsch et al., 2011, 2012).

60 Many previous studies have largely focussed on shallow crustal faults that form at
61 diagenetic temperatures below 200°C. Fault gouges from such environments are assumed to
62 consist of (1) detrital illite/muscovite (2M₁) derived from wall rocks and (2) authigenic or in
63 situ illite (1M/M_d) precipitated within the brittle fault zone during faulting (van der Pluijm et
64 al., 2001; Duvall et al., 2011). Based on a two-end member mixing model, quantified
65 percentages of each illite polytypes (1M and 2M) in different clay size fractions and their
66 apparent ⁴⁰Ar–³⁹Ar ages are used to extrapolate the age of the pure authigenic clay (IAA:
67 Illite Age Analysis approach, e.g., van der Pluijm et al., 2001; Duvall et al., 2011). However,
68 assuming that 2M illite is systematically of detrital origin can be misleading, since the
69 formation of authigenic 2M illite in diagenetic-to-hydrothermal conditions is also reported in
70 the literature (e.g. Lonker and Gerald, 1990; Clauer and Liewig, 2013) and brittle faulting can
71 produce authigenic 2M illite particularly in areas of elevated geothermal gradients or deeper



72 parts of exhumed faults (Zwingmann et al., 2010; Viola et al., 2013; Mancktelow et al.,
73 2015). While successful isotopic dating of brittle faulting and reactivation within single fault
74 core was reported previously (Viola et al., 2013), the present study integrating fault rocks
75 from different depths and locations is a new and challenging approach to help better
76 understand illite crystallisation in gouge during relatively low-temperature brittle fault
77 reactivation episodes in complex Precambrian tectonic settings.

78 **2. GEOLOGICAL SETTING, SAMPLE LOCATIONS AND SAMPLING**

79 The Millungera Basin is a recently discovered sedimentary basin in north Queensland,
80 Australia (Korsch et al., 2011, Fig. 1). It occurs to the east of the Paleoproterozoic Mount Isa
81 Province and is covered by the thin Jurassic–Cretaceous Eromanga-Carpentaria Basin. An
82 angular unconformity between the Eromanga and Millungera Basins indicates that the upper
83 part of the Millungera Basin was eroded prior to deposition of the Eromanga-Carpentaria
84 Basin (Korsch et al., 2011), allowing sampling of the deeper part of the basin, which is
85 strongly deformed and faulted (see below). Interpretation of aeromagnetic data suggests that
86 the basin might have a ~~real~~ dimension of up to 280 km by 95 km (Korsch et al., 2011). Apart
87 from geophysical data, almost no geological information exists on the basin. Prominent thrust
88 fault systems truncate both the western and eastern margins of the basin. Particularly the
89 eastern part of the basin has been cut by several deep-penetrating, northeast-dipping thrust
90 faults, with associated development of hanging wall anticlines. Based on SHRIMP U-Pb
91 geochronology of detrital zircons from the Millungera Basin sandstones, the maximum
92 depositional age of the Millungera Basin is constrained to 1574 ± 14 Ma (Neumann and
93 Kositcin, 2011).

94 Core samples were taken from the lower parts of boreholes Julia Creek 1 (JC) and
95 Dobbyn 2 (Dob) drilled as part of a state (Queensland)-wide geothermal investigation. The



96 wells are 150 km apart (Fig. 1 and Table 1) and intersect the Mesozoic Eromanga-
97 Carpentaria Basin in the upper part. Julia Creek 1 intersected 320.05m of the Eromanga Basin
98 sequence and 179.97m of the Millungera Basin sequence; Dobbyn 2 intersected 332.40m of
99 the Carpentaria Basin sequence and 155.64m of the Millungera Basin sequence. It should be
100 noted that the succession within the Millungera Basin has not been formally defined.
101 According to deep seismic reflection survey, a number of large-scale structures are
102 interpreted to occur as basin-bonding and intra-basin fault systems (see Korsch et al., 2011).
103 Small scale faults and fractures have also been described from logging of the cores extracted
104 from JC and Dob (Faulkner et al., 2012; Fitzell et al., 2012). We collected a total of 9 Julia
105 Creek 1 and 6 Dobbyn 2 fault gouge samples that were all analysed for the <2 µm clay
106 mineral content (Table 1; Supplementary Fig. S1) and some of which have been selected for
107 K–Ar, ⁴⁰Ar–³⁹Ar, and Rb–Sr dating and trace element studies. We also sampled
108 representative host rock samples adjacent to the fault gouge zones (Table 1).

109 3. ANALYTICAL PROCEDURES

110 3.1. Clay characterisation

111 Samples were prepared for clay-fraction separation by gently hand-crushing the rocks to
112 sand size to avoid artificially reducing grain size of detrital/primary mineral components.
113 Samples were then disaggregated in distilled water using an ultrasonic bath. Clay fractions
114 were separated by the sedimentation method (for <2 µm) and centrifugation (for <1 µm
115 subfractions to <0.1 µm). XRD on whole-rock samples and clay separates of different size
116 fractions were carried out (Table 1). The XRD analyses were conducted on a Bruker D4
117 Endeavor and D8 Advance (CoK α and CuK α radiation, respectively), operated at 40 kV and
118 30 mA at a scanning rate of 1°2 θ /min and 0.05°/step. Following XRD analysis of air-dried
119 samples, the oriented clay-aggregate mounts were placed in an ethylene–glycol atmosphere at



120 30–40°C overnight prior to additional XRD analyses. For polytype analyses, clay fractions of
121 random powder from fault gouge samples (if sufficient amount of material was available) were
122 scanned from 16 to 44 °2θ in the step-scanning mode with a step size of 0.05 degrees and a
123 counting time of 30 second per step.

124 Illite polytypes for randomly oriented pure illite samples have been distinguished with
125 the diagnostic peaks suggested by Grathoff and Moore (1996). To determine the $2M_1$ and $1M$
126 and $1M_d$ % contents of illite/muscovites, the ratios of $(2.80 \text{ \AA} - 3.0 \text{ \AA}) / (2.58 \text{ \AA})$ and $(3.07$
127 $\text{ \AA}) / (2.58 \text{ \AA})$ peak areas for $2M_1$ and $1M$, respectively were used, as proposed by Grathoff and
128 Moore (1996). The presence of $1M_d$ illite was detected by the presence of the illite hump around
129 the illite 003 diffraction peak (Grathoff and Moore, 1996). WINFIT decomposition by profile
130 fitting was used for determination of areas of the specific peaks of polytypes. Polytype
131 quantification errors are estimated at about ±5%.

132 The illite crystallinity (IC), or Kübler index, is defined as the width of the first order illite
133 basal reflection (10 \AA peak) at half height and expressed in $\Delta 2\theta$ values. The Kübler index
134 decreases with increasing illite crystallinity (a measure of the ordering/ thickness of illite
135 crystallites), with temperature being the most important controlling factor (Ji and Browne, 2000
136 and references therein). IC is a well-accepted mineralogical indicator of the grade of diagenesis,
137 hydrothermal and low-temperature regional metamorphism (Merriman and Peacor 1999;
138 Merriman and Frey, 1999; Ji and Browne, 2000). However, chlorite crystallinity (ChC) or
139 Arkai Index is becoming an additional or alternative technique (particularly in mafic rocks) to
140 evaluate paleotemperature conditions (Árkai, 1991; Warr and Cox, 2016). The ChC is
141 determined through measurement of chlorite 002 peak width (Árkai, 1991). The IC and ChC
142 results of this study were calibrated against the Crystallinity Index Standard (CIS) scale using
143 the procedure and interlaboratory standards of Warr and Máhlmann (2015).



144 **3.2. Petrographic analysis**

145 The thin sections were first examined under plane-polarized light and cross-polarized
146 light conditions using a Nikon Eclipse LV100N POL and a Zeiss Axio Imager.A2m polarizing
147 microscope polarizing microscope. Further examination of the thin sections was undertaken
148 using a Philips XL 40 scanning electron microscope (SEM) equipped with a X-ray energy-
149 dispersive spectrometry (EDS) system for chemical spot analyses. The sections were analysed
150 using 30 kV accelerating voltage and a working distance of 12 mm. Images were collected in
151 back-scattered electron mode. Additionally, clay separates were carbon coated and examined
152 using an EDS equipped Zeiss Ultra Plus SEM qualitative phase identification. The samples
153 were analysed under high vacuum with a 15 kV accelerating voltage and a working distance of
154 6 mm. Images of clay separate were collected in secondary electron acquisition mode.

155 **3.3. Rb–Sr illite dating**

156 For the Rb–Sr dating (conducted at the Radiogenic Isotope Facility laboratory RIF, the
157 University of Queensland (UQ)), illitic clay separates were leached for 15 min at room
158 temperature in 1 N distilled HCl (Clauer et al., 1993). Leachate and residue were separated by
159 centrifuging. The residue was rinsed repeatedly with milli-Q water, dried and reweighed. Acid
160 leached residues and untreated samples were measured directly by Thermo X-series 1
161 quadrupole ICP–MS with precision better than 0.5% (1σ). The Sr-enriched fraction was
162 separated using cation exchange resins. Sr isotopic ratios were measured on a VG Sector-54
163 thermal ionisation mass spectrometer (TIMS). Sr was loaded in TaF₅ and 0.1 N H₃PO₄ on a
164 tantalum or tungsten single filament. Sr isotopic ratios were corrected for mass discrimination
165 using $^{86}\text{Sr}/^{88}\text{Sr} = 0.1194$. Long-term (6 years) reproducibility of statically measured NBS SRM
166 987 (2σ ; $n = 442$) is $^{87}\text{Sr}/^{86}\text{Sr} = 0.710249 \pm 0.000028$. More recent dynamically measured



167 SRM 987 had $^{86}\text{Sr}/^{88}\text{Sr}$ ratios of 0.710222 ± 0.000020 (2σ ; $n = 140$). Rb–Sr isochron ages were
168 calculated using the ISOPLOT program (Ludwig, 2012).

169 **3.4. K–Ar illite dating**

170 The K–Ar dating was performed at the CSIRO Argon facility in Perth, Australia
171 according to standard methods given in detail by Dalrymple and Lanphere (1969). Potassium
172 content was determined by atomic absorption. The error of K determination of standards is
173 better than 2 %. The K blank was measured at 0.50ppm. Argon was extracted from the
174 separated mineral fraction by fusing the sample within a vacuum line serviced by an on-line
175 ^{38}Ar spike pipette. The isotopic composition of the spiked Ar was measured with a high
176 sensitivity, on-line, VG3600 mass spectrometer. The ^{38}Ar was calibrated against standard
177 biotite GA1550 (McDougall and Roksandic, 1974). Blanks for the extraction line and mass
178 spectrometer were systematically determined and the mass discrimination factor was
179 determined periodically by airshots (small amounts of air for $^{40}\text{Ar}/^{36}\text{Ar}$ ratio measurement).
180 During the course of the study, 16 international standards (8 HD-B1 and 8 LP-6) and 16 airshots
181 (small amounts of air for $^{40}\text{Ar}/^{36}\text{Ar}$ ratio measurement) were analyzed. The results are
182 summarized in Table 2. The error for the $^{40}\text{Ar}/^{36}\text{Ar}$ value of the airshot yielded 296.08 ± 0.23 .
183 The general error for argon analyses is below 1% (2σ) based on the long-term precision of Ar
184 measurements of the international standards. The K–Ar age was calculated using ^{40}K abundance
185 and decay constants recommended by Steiger and Jäger, (1977). The age uncertainties take into
186 account the errors during sample weighing, $^{38}\text{Ar}/^{36}\text{Ar}$ and $^{40}\text{Ar}/^{38}\text{Ar}$ measurements and K
187 analysis.

188 **3.5. ^{40}Ar – ^{39}Ar illite dating**

189 Four fault gouge illites were dated by the ^{40}Ar – ^{39}Ar method at the University of
190 Michigan. Illitic clay samples were re-suspended in 1 ml of deionized water, spun-down at



191 10,000 rpm in a microcentrifuge and carved into a ~1 mm pellet following decanting. To avoid
192 loss of ^{39}Ar due to recoil, clay pellets were placed in 1 mm ID fused silica vials prior to being
193 sent for neutron irradiation for 90 MWh in medium flux locations of the McMaster Nuclear
194 Reactor (hole 8C for irradiation 1, 8A for irradiation 2). Following irradiation, samples were
195 attached to a laser fusion system, the vials were broken under a 1×10^{-8} Torr vacuum, and the
196 samples step-heated in situ using a defocused beam from a 5 W Coherent Innova continuous
197 Ar-ion laser operated in multi-line mode. Argon isotopes were then analyzed using a VG1200S
198 mass spectrometer equipped with a Daly detector operated in analogue mode using methods
199 by Hall (2014). Ages in this study are calculated relative to an age of 520.4 ± 1.7 Ma for standard
200 hornblende MMhb-1 (Samson and Alexander, 1987). The total gas age obtained from the
201 vacuum encapsulated sample is equivalent to a conventional K–Ar age and quoted at 1σ .

202 **3.6. Illite trace element analysis**

203 For trace element analysis conducted in the Radiogenic Isotope Laboratory at the
204 University of Queensland (RIF, UQ), clay samples were dissolved with a mixture of HF and
205 nitric acids on a hotplate, then evaporated to dryness, refluxed twice with nitric acid and
206 dissolved in 2N nitric acid. Aliquots of the solutions were spiked with internal standards,
207 diluted and analysed on a Thermo X-series 1 quadrupole inductively coupled plasma mass
208 spectrometer (ICP-MS). Sample preparation and analytical procedures used were similar to
209 those of Eggins et al. (1997), except that Tm was not used as an internal standard and duplicate
210 low-pressure digestions of US Geological Survey W-2 diabase standard and a known
211 concentration profile (pre-analysed by laboratory) were used for calibration (Li et al., 2005)
212 were used as the calibration standard. . The $^{156}\text{CeO}/^{140}\text{Ce}$ ratio for the run was 0.016. Long-
213 term precision (RSD) was based on duplicate analyses of the duplicate digestions of AGV1,
214 whilst precision for the run was based on five duplicate analyses of W-2 which were better than



215 3% for most elements, except for Li, Zn, Mo, Cd, and Cs, which ranged between 5% (Li, Cd
216 and Cs) and 15% (Zn).

217 4. RESULTS

218 4.1 Sample description and micro structures

219 4.1.1 Core descriptions

220 The undifferentiated Millungera sequence intersected in Julia Creek 1 and Dobbyn 2
221 comprises medium to coarse-grained, pink to dark red quartzose sandstone with minor
222 interbeds of micaceous clay siltstone and claystone. These sandstone intervals are fractured
223 and faulted throughout the sequence and show evidence of pervasive hydrothermal alteration,
224 particularly near the cracks (Fig. 2a, see also Faulkner et al., 2012; Fitzell et al., 2012).
225 Alteration products are very fine-grained clay-rich material that contain angular clasts from
226 the main rock (Fig. 2b). Clay-rich layers show mostly different colour (grey-beige-red)
227 relative to the sandstone wallrock (Fig. 2b-e). Numerous open cracks coated with green clay
228 are observed throughout cores (Fig. 2c). The clay rich material occurs along the fault planes
229 and in cracks as single vein or complex network of partially consolidated material (Fig. c-d).
230 They also exist as relatively thick layers (up to 30 cm) within the sandstone cores (Fig. 2e),
231 with a sharp transition the host rock (Fig. 2a-f) and contain commonly slickenside surfaces at
232 the contact with the host rock (Fig. 2f-h).

233 4.1.2 Petrographic and micro-structural analysis

234 Thin section photomicrographs and SEM images of representative samples are shown
235 in Fig. 3a-f. Microscopic observations show that the undeformed host rock sandstones consist
236 of mainly quartz, some muscovite and minor K-feldspar. Petrography, in combination with
237 XRD analysis show that kaolinite, illite, and chlorite are present as a pore and fracture-filling



238 cement in the sandstones (Fig. 3a-b), while detrital mica occurs in large elongate grains with
239 alteration in illite along its edges (Fig. 3b). Chlorite does not show any coarse detrital grains
240 and only occurs authigenetically in very fine-grains dispersed and mixed with illites as pore-
241 filling mineral phases (Fig. 3a).

242 Faulted specimen from Julia Creek 1 show a characteristic S-C foliation (e.g. Berthe et
243 al., 1979) under the optical microscope (Fig. 4a, b and c) with an anastomosing network of
244 phyllosilicate defining the C shear oriented parallel to the shear direction. The S- shears
245 include planes of insoluble minerals oriented oblique to the sense of shear (Fig. 4c) and
246 quartz fragments embedded in a fine-grained illite-rich matrix as shown by electron
247 microscopy imaging (Fig. 4d and e). These quartz grains have angular shape with intensely
248 serrated grain boundaries and are slightly elongated with their long axis parallel to the
249 orientation of the S- surface. Booklets of kaolinite partially replaced by illite are also visible
250 in the deformed specimens (e.g. Fig. 4d and e).

251 Faulted hand specimens from Dobbyn 2 exhibit planar to slightly arcuate fault surfaces
252 with a high gloss and display evident slickenside surfaces decorated by short-wavelength
253 (200-500 μm) striations (Fig. 5a). Sense of shearing and offset on the faults are difficult to
254 assess due to lack of markers visible in the cores. Domains of foliated and brecciated
255 cataclasite can be distinguished on hand specimen (Fig. 5b) and in thin section (Fig. 5c). Both
256 domains are characterised by hematite rich injection veins emanating from the slip surfaces
257 and oriented at approximately right angle to them with sharp contacts with the surrounding
258 material (Fig. 5 d, e). The domains and are bounded by sharp contacts defined by slickenside
259 surfaces constituted by thin layers (50-100 μm thick) of iso-oriented phyllosilicates (Fig. 5d,
260 f). The foliated cataclasite domains are characterised by a set of conjugate shears referred to
261 as S-C-C' structures visible at the micro-scale using scanning electron microscopy (Fig. 5e).



262 Oblique to the shear direction S surfaces are defined by the preferred alignment of elongated
263 clasts of phyllosilicates and are oriented approximately perpendicular to the maximum
264 flattening of the strain ellipsoid.

265 C and C' represent discrete shear surfaces, the former is parallel to the macroscopic slip
266 surface and the latter deflects the S foliation by disrupting the grains into an ultrafine grained
267 oriented at a small angle ($\sim 20^\circ$) to the macroscopic shear surface but with the opposite sense
268 of obliquity relative to the S-surfaces (Fig. 5e). The cataclasite domain show the original rock
269 fabric of detrital quartz grains and pore-filling diagenetic kaolinite disrupted by a pervasive
270 network of hematite filled intragranular micro-fractures (Fig. 5g).

271 4.1.3. XRD and SEM clay mineral analysis

272 Illite is the most abundant clay mineral in the majority of samples, with kaolinite and
273 chlorite being present in many samples. The latter minerals are more abundant than illite in
274 sample Dob-449.3 (Table 1; Supplementary Fig. S1). XRD analysis shows that 001 peak
275 position of the illite does not change after ethylene glycol treatment, which indicates that the
276 amount of smectite-like clays is insignificant (Srodon and Eberl, 1984). IC measurements for
277 $<2 \mu\text{m}$ size fractions normalised to the standards of Warr and Rice (1994) range from 0.17 to
278 1.00 $\Delta 2\theta$ and from 0.46 to 1.01 $\Delta 2\theta$ for samples from Dobbyn 2 and Julia Creek 1,
279 respectively (Table 1). We also measured IC values of $>2 \mu\text{m}$ size fractions of some fault
280 gouge samples. Such non-clay fractions contain mostly parallel- oriented mica-type
281 inherited/detrital minerals representing the pre-fault protolith to compare their metamorphic
282 grade with that of the fault gouges. Coarser $2 \mu\text{m}$ size fractions of samples JC-408, Dob-
283 389.6, Dob-441, Dob-449.3, and Dob-476.6 IC give values of 0.42 $\Delta 2\theta$, 0.36 $\Delta 2\theta$, 0.14 $\Delta 2\theta$,
284 and 0.26 $\Delta 2\theta$, respectively. Smaller $2 \mu\text{m}$ size fractions of the host rock IC values range
285 between 0.20 and 0.27 $\Delta 2\theta$, and 0.46 and 0.51 $\Delta 2\theta$ for Dobbyn 2 and Julia Creek 1 samples,



286 respectively (Table 1). The normalised chlorite crystallinity values (ChC) of $<2\ \mu\text{m}$ for
287 samples free of kaolinite range from 0.35 to 0.42 $\Delta 2\theta$ (Table 1).

288 Non-oriented random powder XRD analysis of $<2\ \mu\text{m}$, 2-1 μm , $<1\ \mu\text{m}$, and $<0.5\ \mu\text{m}$
289 fractions for samples from borehole Julia Creek 1 (JC) confirm the mixture of 2M, 1M,
290 and $1M_d$ polytypes of illite, while samples from borehole Dobbyn 2 consist of largely 2M
291 illite with some $1M_d$ illite up to 20% for some samples (Table 1, Supplementary Fi. S1). SEM
292 analysis show 2M illites forming large euhedral crystal plates with sharp edges that occur
293 together with smaller 1M/ $1M_d$ illite plates (Fig. 3c-f). A number of previous studies (e.g.,
294 Clauer and Liewig, 2013) showed that detrital illitic clay particles rarely have straight edges
295 like those presented in this study, but rather occur in particles with diffuse-blurred and
296 irregular edges (Fig. 3c, the white material on the right-hand site). Samples Dob-441 and
297 Dob-476.6 have generally larger crystal size (Fig. 3c-d) than samples JC-408 and JC-360.7
298 (Fig. 3c-d). The abundancy of 2M illite represented by these larger crystal plates in samples
299 Dob-441 and Dob-476.6 is confirmed by XRD random powder polytype analysis (Table 1;
300 Supplementary Fig. S1). Dob samples however, are poorly sorted in terms of crystal size
301 distribution with the presence of a number of much smaller crystals (Fig. 3c-d). Such small
302 crystals are mostly rounded (see the arrow in Fig. 3d) and probably represent the $1M_d$ illite
303 recorded in random powder XRD pattern of sample Dob-441. It is apparent that larger crystal
304 plates were formed by coalescence of smaller crystals through Ostwald ripening (Eberl et al.,
305 1990) (e.g., dashed arrows in Fig. 3d).

306 4.2. Illite geochronology

307 4.2.1. ^{40}Ar - ^{39}Ar dating

308 Four fault gouge illite samples of $<2\ \mu\text{m}$ fraction were analysed for ^{40}Ar - ^{39}Ar
309 geochronology (Table 1 and Fig. 6). Based on their illite crystallinity values, these samples



310 represent high diagenetic to upper anchizonal metamorphic grade with 2M illite varying
311 between 62% and 100%. Samples had 0.050%–0.12% low temperature ^{39}Ar recoil loss,
312 which is characteristic of well crystallised illite grains (Hall et al., 1997). Age data (1σ) is
313 obtained as total gas ages (Table 1 and Fig. 6) (cf., Dong et al., 1995). Samples JC-360.7, JC-
314 408, Dob-441, and Dob-446.6 yield total gas of 1038.1 ± 2.9 Ma and 1099.6 ± 3.0 Ma,
315 1040.0 ± 2.3 Ma and 1106.8 ± 2.5 Ma (Table 1; Fig. 6). The analyses do not show well
316 developed plateaux, which can be explained by recoil and varying ages of individual crystals
317 (cf., Clauer et al., 2012).

318 4.2.2. *K–Ar dating*

319 K–Ar ages of fault gouge and sandstone illites of different size fractions from $>2 \mu\text{m}$ to
320 $<0.1 \mu\text{m}$ from boreholes Julia Creek 1 and Dobbyn 2 are presented in Table 3 and Fig. 7. A
321 histogram of all K–Ar results obtained from gouge zones are shown in Fig. 7a. K–Ar size
322 fraction ages for fault gouge and host rock matrix illite and their interpretation in relation to
323 the tectonic history are shown in Fig. 7b and Fig. 7c, respectively. Due to sample nature it
324 was not possible to extract sufficient material for $<0.1 \mu\text{m}$ or $<0.5 \mu\text{m}$ fractions from some
325 fault rock samples, especially from those samples from Dobbyn 2 with illites with low IC
326 values ($0.42 \Delta 2\theta$ or lower for $<2 \mu\text{m}$).

327 Size fractions from $<2 \mu\text{m}$ to $<0.1 \mu\text{m}$ of fault gouge samples JC-343, JC-360.7, and
328 JC-440.5 from Julia Creek 1 yield consistent ages (Table 1) with a mean (average) of 1036.2
329 ± 9.7 Ma, 1025 ± 17.7 Ma, 1028.9 ± 17.3 Ma (1 s.d.), respectively. The mean age of $1025 \pm$
330 17.7 Ma for sample JC-360.7 is identical with the Ar–Ar total gas age of 1038.1 ± 2.9 Ma of
331 $<2 \mu\text{m}$ of the same sample. Various size fractions from $2\text{--}1 \mu\text{m}$ to $<0.5 \mu\text{m}$ of another fault
332 gouge sample from Julia Creek 1 (JC-408) give also consistent but older ages with a mean of
333 1114.2 ± 6.9 Ma. However, $^{40}\text{Ar}\text{--}^{39}\text{Ar}$ total gas age of sample JC-408 is 1040.0 ± 2.3 Ma,



334 which is identical to the above mentioned ages of JC-343, JC-360.7, and JC-440.5 samples
335 (Table 1; Fig. 7a). The $>2 \mu\text{m}$ fraction of sample JC-408 yields, by contrast, a distinctively
336 different and older K–Ar of $1243.2 \pm 29.1 \text{ Ma}$ (Table 1; Fig. 7a).

337 K–Ar ages of different fault gouge illites from Dobbyn 2 are more variable (Fig. 5a). 2-
338 $1 \mu\text{m}$, <2 , $1\text{-}0.5 \mu\text{m}$, and $0.5\text{-}0.1 \mu\text{m}$ fractions of sample Dob-389.6 yield consistent ages
339 (Table 1; Fig. 7a) with a mean of $1061 \pm 19.5 \text{ Ma}$, whereas $<0.5 \mu\text{m}$ and $<0.1 \mu\text{m}$ give
340 younger ages of $981.8 \pm 22.6 \text{ Ma}$ and $905.4 \pm 20.9 \text{ Ma}$, respectively.

341 Smaller 2 and $<1 \mu\text{m}$ fractions of fault sample Dob-441 give inconsistent but close K–
342 Ar ages of $1148.7 \pm 26.9 \text{ Ma}$ and $1086.5 \pm 25.1 \text{ Ma}$, respectively. The $^{40}\text{Ar}\text{--}^{39}\text{Ar}$ total gas age
343 of $1068.1 \pm 1.8 \text{ Ma}$ for this sample is consistent with the K–Ar age of $1086.5 \pm 25.1 \text{ Ma}$ of
344 the $<1 \mu\text{m}$ fraction. A significantly older K–Ar age of $1312.3 \pm 30.7 \text{ Ma}$ is obtained for the
345 $>2 \mu\text{m}$ fraction of sample Dob-441 (Table 1; Fig. 7a).

346 Samples Dob-449.1 and Dob-449.3 were taken from a clay-rich fault rock zone, with
347 the former and latter representing beige-light grey and hematite-rich red varieties,
348 respectively. The $2\text{-}0.5 \mu\text{m}$, $<2 \mu\text{m}$, $1\text{-}0.5 \mu\text{m}$, and $<0.5 \mu\text{m}$ fractions of sample Dob-449.1
349 yield younger but concordant ages with a mean of $922.4 \pm 19.9 \text{ Ma}$. However, illite fractions
350 of sample Dob-449.3 (just 20 cm below) yield scattering K–Ar ages regardless of the grain
351 size. K–Ar ages of size fractions $2\text{-}1 \mu\text{m}$, $1\text{-}0.5 \mu\text{m}$, $0.5\text{-}0.2 \mu\text{m}$, and $<0.5 \mu\text{m}$ for sample
352 Dob-449.3 are $1047.7 \pm 24.2 \text{ Ma}$, $1117.2 \pm 25.8 \text{ Ma}$, $950.9 \pm 22.0 \text{ Ma}$, and $1004.4 \pm 23.2 \text{ Ma}$,
353 respectively. Coarser $2 \mu\text{m}$ fraction being rich in detrital mica gives a much older age of
354 1259.0 ± 29.1 (Table 1; Fig. 7a).

355 K–Ar age of $2\text{-}1 \mu\text{m}$ fraction and K–Ar and $^{40}\text{Ar}\text{--}^{39}\text{Ar}$ total gas ages of $<2 \mu\text{m}$ fraction
356 of the deepest fault rock sample from Dobbyn 2 (Dob-476.6) yield identical ages within



357 analytical errors of 975.7 ± 22.2 Ma, 983.7 ± 23.0 Ma, and 994.6 ± 2.2 Ma, respectively, with
358 a mean of 984.7 ± 9.5 Ma. A much older age of 1170.4 ± 27.4 Ma is obtained for >2 μm
359 fraction of this sample (Table 1; Fig. 7a).

360 K–Ar and ^{40}Ar – ^{39}Ar results of all size fractions (except >2 μm) from fault gouges listed
361 in Table 1 are presented as a histogram and probability density distribution plot (Fig. 7b).
362 Isotopic dates define distinct age clusters at ~ 1070 Ma, ~ 1040 Ma, and ~ 995 Ma. There are
363 also less pronounced, but noticeable age clusters at ~ 1115 Ma and ~ 905 Ma (Fig. 7b).

364 K–Ar ages of different size fractions of illitic clay minerals that occur as matrix in
365 undeformed, adjacent sandstones (see Figs. 2 and 3) are also presented in Table 1 and Fig. 7c.
366 Three different size fractions of three different samples, Dob-449.4, JC-500, and JC-360.6,
367 yield same ages within error, averaging at 1047 ± 21 Ma, 1079 ± 13 Ma, 1062 ± 7 Ma (1 s.d),
368 respectively (Table 1 and Fig. 7c). The <0.2 fine fractions of JC-360.6 and JC-500 yield
369 within error identical younger ages of (928.3 ± 47.6 and 878.3 ± 45.1 , respectively), which
370 might indicate cessation of illite formation or partial reset due to final faulting with the Early
371 Neoproterozoic deformation events and associated fluid flow.

372 4.2.3. Rb–Sr isochron dating

373 Rb–Sr data for the untreated, acid-leached residues, and leachates of different <2 μm
374 clay fractions for the fault gouge illites collected from different stratigraphic levels in Julia
375 Creek 1 and Dobbyn 2 are presented in Table 4 and on Fig. 8. The data show three parallel
376 well-defined linear relationships indicating similar isochron ages, but with different initial
377 $^{87}\text{Sr}/^{86}\text{Sr}$ values (Fig. 8a). Some samples plot off these lines, possibly because they have
378 different initial $^{87}\text{Sr}/^{86}\text{Sr}$ values, and these samples are not considered for isochron age
379 calculation. Samples from Dobbyn 2 plot on the two upper isochron lines with higher
380 $^{87}\text{Sr}/^{86}\text{Sr}$ initial values (Fig. 8a). Residue of samples JC-360.7B <0.5 μm plot also on one of



381 these lines (the middle line on Fig. Fig. 8a). All other Julia Creek 1 define a separate Rb–Sr
382 isochron line with lower $^{87}\text{Sr}/^{86}\text{Sr}$ initial values (the lower line on Fig. 8a).

383 Leachates are accessory acid-soluble non-silicate phases (mostly carbonate minerals
384 and amorphous grain coatings of FeO(OH) (Clauer et al., 1993). However, Rb–Sr isotopic
385 systematics of the acid-soluble leachate is not in equilibrium with that of the illites, since the
386 leachates plot off the Rb–Sr lines. Lower $^{87}\text{Sr}/^{86}\text{Sr}$ values of the leachates (mostly <0.72) in
387 comparison to highly radiogenic (elevated) initial $^{87}\text{Sr}/^{86}\text{Sr}$ of illites indicate interaction of
388 rocks with some late stage fluids from which acid-soluble non-silicate phases were formed.

389 The data of untreated and residues of <2 μm fractions from Julia Creek 1 samples
390 define a linear relationship from which the slope yields a Rb–Sr errorchron age of 1041 ± 46
391 Ma (initial $^{87}\text{Sr}/^{86}\text{Sr} = 0.7194 \pm 0.0011$, MSWD=27) (Fig. 8b). However, as apparent from the
392 $^{87}\text{Rb}/^{86}\text{Sr}$ vs. $^{87}\text{Sr}/^{86}\text{Sr}$ plot on the Fig. 8a-b, untreated aliquots of samples JC-387.8 and JC-
393 440.5 plot slightly at the lower part of the line leading to a large analytical error and MSWD
394 value. This is probably caused by the effect of the leachable components that were not in
395 isotopic equilibrium with the clays, as discussed above. When these two untreated samples
396 are omitted, the data scatter is reduced significantly with a well-defined regression line
397 (MSWD=2.3) and corresponding isochron age of 1023 ± 12 Ma (initial $^{87}\text{Sr}/^{86}\text{Sr} =$
398 0.72009 ± 0.00025) (Figure 8c). Residue and untreated aliquots of <2 μm fractions from Dob-
399 449, Dob-441A, and Dob-389.6, and residue of JC-360.7B <0.5 μm yield an analytically
400 indistinguishable age of 1033 ± 25 Ma (initial $^{87}\text{Sr}/^{86}\text{Sr} = 0.72326 \pm 0.00094$; MSWD=2.5)
401 (Fig. 8d). A somewhat younger Rb–Sr age of 1000 ± 12 (initial $^{87}\text{Sr}/^{86}\text{Sr} = 0.72841 \pm 0.00030$,
402 MSWD = 0.065) was obtained for Dob-476.6 <2 μm (untreated and residue), Dob-389.6 2-1
403 μm and 0.5-0.1 μm (residue) (Fig. 8e).

404 4.3. Trace elements



405 Rare earth element (REE) data and Th, U, and Sc contents of illites (<2 μm clay-size
406 fractions) from the fault gouge samples are given in Table 4. Chondrite-normalised REE
407 patterns of illites from the fault gouges are shown in Fig. 9a. In addition, the REE pattern of
408 Post-Archean Average Shale (PAAS, Taylor and McLennan, 1985) is included in the REE
409 diagram. The fault gouge illites are substantially enriched in light REE (LREE) relative to
410 PAAS with La contents as high as 10xPAAS. The illites are however, somewhat depleted in
411 heavy REE (HREE) relative to LREE (Fig. 9a). The chondrite-normalised $(\text{La}/\text{Lu})_c$ ratios of
412 the illites are significantly higher (up to 76) than the $(\text{La}/\text{Lu})_c$ ratio of PAAS (10) (Table 4).
413 Fault gouge illites are also enriched in Th and U (up to 10 times) in comparison to PAAS
414 (Table 4).

415 5. DISCUSSION

416 5.1. Faulting, fluid-rock interactions and clay generation

417 Brittle deformation and faulting is evident from cores in the sampled intervals in Julia Creek
418 1 and Dobbyn 2, probably associated with the large scale faults inferred from interpretations
419 of seismic survey (Fig. 1). Under upper crustal conditions, fault zones accommodate intense
420 shear strain often localised in bands of cataclastic deformation formed by friction-dominated
421 faulting within the seismogenic regime (Sibson, 1977; Schmid and Handy, 1991). While
422 cataclastic fault rocks are generally considered to display random fabric, foliated fault rocks
423 such as fault gouge and foliated cataclasites have also been reported in different lithologies
424 ranging from crystalline rocks to siliciclastic and carbonate dominated sediments (Chester et
425 al., 1985; Rutter et al., 1986; Lin, 1999; Ujiie et al., 2007; Laurich et al., 2004; Delle Piane et
426 al., 2017; Nicchio et al., 2018). Frictional sliding and abrasion are common processes during
427 repeated fault movement and result in strong grain size reduction of the fault rocks with
428 respect to the constituting minerals in the undeformed portion of the host rocks. The abundant



429 presence of micro and nano-sized particles in cataclasites and gouges may result from
430 combined effects of cataclasis and pressure solution-precipitation during deformation in the
431 presence of fluids (e.g. Vrolijk and van der Pluijm, 1999; Solum et al., 2005). The corroded
432 grain boundaries of quartz grains in faulted samples from Julia Creek 1 (Fig. 4) and the
433 presence of the injection veins and hydrothermal hematite in the cataclasites from Dobbyn 2
434 (Fig. 5) indicates that deformation occurred in a fluid-rich environment that promoted detrital
435 muscovite dissolution and new growth of illite. The small injections veins that are observed
436 to cut through the foliated cataclasites and the detrital quartz grains (Fig. 5) may represent the
437 effect of hydraulic fracturing due to a fast increment of fluid pressure in the fault zone during
438 a seismic slip (e.g. Sibson, 1989; Cowan et al., 2003; Ujiie et al., 2007; Rowe et al., 2012). At
439 the core scale, some samples show no shearing-related fabrics in the sandstone cores (fresh
440 and hard) adjacent to clay-filled cracks (Fig. 2a-d). This may be a result of the precipitation
441 of clay-rich material and injection of granular material from seismically-mobilised circulating
442 fluids.

443 K–Ar results show that illites from fault gouges and matrix illites in undeformed adjacent
444 sandstones precipitated contemporaneously (Fig. 7). In some tectonically active regions,
445 mineral assemblages from the fault rocks and their parent rocks are significantly different,
446 whereby parent rocks do not contain any alteration minerals with new mineral growth being
447 restricted to the fault rocks. This indicates that the heat and fluid flows associated with
448 mineral authigenesis were not controlled by regional tectonic events in these regions, but
449 rather confined to the areas within the fault zone (e.g., Uysal et al. 2006; Isik et al., 2014;
450 Babaahmadi et al., 2019). However, the relation between large-scale fluid flow and seismic
451 events has long been reported (e.g., Bruhn et al., 1994; Eichhubl et al., 2010; Faulkner et al.,
452 2010; Lupi et al., 2010 and references therein). Brittle faulting in the upper crust involves
453 episodic changes in the stress level that can expel large volumes of fluids, leading to the



454 generation of hydrothermal/geothermal systems. Faults and veins and their immediate
455 surrounds represent zones of fluid passage and transfer of mass through those fluids (e.g.,
456 Sibson, 1987). Mineral alteration in slip zone gouge extends outward from the fault zone into
457 the undeformed wall rock (e.g., Parry et al., 1991; Craw et al., 2009). The wall rock
458 alteration is attributed to the diffusion and advection of fluids, and hence chemical mass and
459 heat transfer associated with deformation. For example, metasomatic alteration zones
460 develop around fluid pathways by advection with mineral dissolution and precipitation
461 increasing towards the conduit and dictated by infiltrating fluids (Ferry and Dipple, 1991).
462 Metasomatic mineral alteration is common in sedimentary basins contemporaneous with
463 regional extensional tectonics. Alteration is driven by reactivity of sandstone host rocks with
464 illitic clay minerals, K-feldspar (adularia), hematite, calcite, and quartz being some common
465 minerals precipitating from tectonically mobilised K-bearing basin brine (Fedo et al., 1995;
466 Michalski et al., 2007; Eichhubl et al., 2010). Similarly, in this study, sandstone immediately
467 above or below the fracture and shear (fault gouge) zones represents zones of alteration of
468 detrital minerals to illite by tectonically moved fluids.

469

470 **5.2. Geochronology: comparison between Rb–Sr, K–Ar and ^{40}Ar – ^{39}Ar ages**

471 Fault gouges from the Millungera Basin in Australia (Fig. 1) contain a mixture of
472 coevally formed 1M/1M_d and 2M illite from which the crystallisation age was determined by
473 a combined application of Rb–Sr, ^{40}Ar – ^{39}Ar , and K–Ar techniques. It is demonstrated that
474 applying both the Rb–Sr and K–Ar (^{40}Ar – ^{39}Ar) techniques for dating the same fault gouge
475 minerals provides more robust and complementary age constraints on faulting episodes and
476 minimises the inherent disadvantages for each isotopic system. A common drawback of Ar
477 geochronology when dating white mica is that Ar apparent ages are either significantly older
478 or younger than the Rb–Sr isochron ages of the same samples (Kelley, 2002; Di Vincenzo et



479 al., 2006). Rb–Sr isotopic systematics may remain unaffected because Rb–Sr resetting
480 requires higher closure temperatures and sufficient fluids in the system to facilitate
481 recrystallisation (e.g., Di Vincenzo et al., 2006). However, a potential pitfall of Rb–Sr dating
482 technique could result from heterogeneous initial $^{87}\text{Sr}/^{86}\text{Sr}$ ratios on a mineral-scale (cf.,
483 Davidson et al., 2005). In this study, as discussed in section in section 4.2.3, we minimised
484 the effect of mineral-scale initial isotopic heterogeneity by analysing different aliquots
485 (untreated, leachates, and residues) and different sub-size fractions of one clay sample.
486 Indeed, different sub-size fractions and aliquots of some samples plot on different isochron
487 lines indicating different $^{87}\text{Sr}/^{86}\text{Sr}$ ratios (Fig. 8, see the discussion below).

488 Illites from the Millungera Basin fault gouges display well-developed linear data arrays
489 on Rb–Sr isochron diagrams with statistically valid late Mesoproterozoic ages (Fig. 8). Such
490 linear relations for fault gouge clays representing acid-leached residue and untreated aliquots
491 and consisting of both 2M and 1M illite can be interpreted as unequivocal indication of a
492 complete isotopic equilibration of the entire illite population during episodic fluid flow
493 episodes controlled by deformation events (cf. Mutlu et al., 2010; Isik et al., 2014; Middleton
494 et al., 2014; Rosenbaum et al., 2015; Babaahmadi et al., 2019). The Rb–Sr isochron ages
495 (1041 ± 46 Ma and 1023 ± 12 Ma) for <2 μm fractions of samples JC-360.7, JC-440.5 (Fig.
496 8b-c) are consistent with K–Ar and for ^{40}Ar – ^{39}Ar (sample JC-360.7) ages of the same fraction
497 and all other different size fractions of the same samples (Table 1 and Fig. 7). Similarly, the
498 Rb–Sr isochron age of 1033 ± 25 Ma for <2 μm fraction of sample Dob-389.6 (Fig. 8d) is
499 concordant with the same size fraction, and 1–0.5 μm and 0.5–0.1 μm fractions of this sample
500 (Table 1 and Fig. 7). Smaller 2 μm fractions of samples Dob-441A and Dob-449.1 in addition
501 plot on the same Rb–Sr isochron in Fig. 8d, with consistent ^{40}Ar – ^{39}Ar age (1068.1 ± 1.8 Ma)
502 and K–Ar ages of <1 μm and <0.5 μm fractions of Dob-441. However, <2 μm of Dob-441
503 yield an older K–Ar age (1148.7 ± 26.9 Ma) (Table 1 and Fig. 7). Unlike the Rb–Sr isochron



504 age (Fig. 8d), K–Ar ages of all different size fractions for sample Dob-449.1 are lower (925
505 to 913 Ma, Table 1 and Fig. 7). The Rb–Sr isochron age of 1000 ± 12 Ma for $<2 \mu\text{m}$ of
506 sample Dob-476.6 (along with the acid-leached residues of Dob-441B and Dob-389.6 for 2-
507 $0.5 \mu\text{m}$ to $0.5\text{-}0.1 \mu\text{m}$ fractions) is consistent with K–Ar ages of the same sample for various
508 size fractions (922.2 ± 21.2 to 983.7 ± 23.0 Ma) within analytical errors (Table 1 and Fig. 7).

509 In summary, most samples with their various size fractions yield consistent Rb–Sr
510 isochron and individual K–Ar ($^{40}\text{Ar}\text{-}^{39}\text{Ar}$) ages. This finding is similar to those reported by
511 some recent studies that presented robust and comprehensive Rb–Sr, $^{40}\text{Ar}\text{-}^{39}\text{Ar}$, and K–Ar
512 age data for high diagenetic and anchizonal fault gouge illites (e.g., Middleton et al., 2014;
513 Rosenbaum et al., 2015; Babaahmadi et al., 2019). Discrepancy in Rb–Sr and K–Ar ages for
514 few samples, e.g., Dob-441 $<2 \mu\text{m}$ (K–Ar age is older) and Dob-449.1 (K–Ar ages are
515 younger), may result from sample heterogeneity (hand-specimen and micro scale, see Figs. 4
516 and 5) presented by more than one illite generation due to multiple faulting episodes. Mixing
517 of different generations is possible in small scale as a result of variable degrees of isotopic
518 resetting of a single illite generation during subsequent faulting events. Pervasive
519 overprinting and re-crystallization can be hindered even in micro scale, which may result
520 from a lack of permeability and/or limited availability of fluids (e.g., Bröcker et al., 2013).

521 **5.3. Implication of Sr isotope and trace element compositions for the evolution of fault-** 522 **related fluids**

523 The trace element composition of authigenic clay minerals reflects the mineral/fluid
524 partition coefficients for different elements, as well as the composition of fluids from which
525 the clays precipitated. Trace element contents and concentrations, as well as some element
526 ratios, can be used to trace the origin of basinal and hydrothermal fluids (e.g., Uysal and
527 Golding, 2003; Uysal et al., 2005; Uysal et al., 2011). The fault gouge illites analysed in this



528 study are highly enriched in LREE and other incompatible elements such as Th and U
529 relative to PAAS (Fig. 9a and Table 4). This geochemical characteristic indicates
530 precipitation of the illites from fluids that must have interacted with rocks of the upper crust
531 enriched in incompatible and heat producing elements. This is also consistent with initial
532 $^{87}\text{Sr}/^{86}\text{Sr}$ values of fault gouge illites that reflect Sr isotope composition of fluids from which
533 the illites precipitated. The radiogenic initial $^{87}\text{Sr}/^{86}\text{Sr}$ ratios of about 0.72 indicate the
534 involvement of fluids that equilibrated with old Rb-rich crustal rocks. The trace element and
535 Sr isotope data are in agreement with seismic and potential field data by Korsch et al. (2011),
536 which is interpreted as indicating the occurrence of granites with a thickness up to 5.5 km
537 below the Millungera Basin. The inferred granites may be a part of the granite (Williams
538 Supersuite) exposed just to the west in the Mt Isa Inlier, which is enriched in Th, U, and K
539 (Korsch et al., 2011 and references therein).

540 Different $^{87}\text{Sr}/^{86}\text{Sr}$ initial values of illites of the parallel isochron lines corresponding to
541 the same Rb–Sr age in Fig. 8 and scatter of Rb–Sr data points for some samples indicate
542 separate circulation pathways for seismically mobilised fluids that that might have restricted
543 to unconnected fault planes and fracture systems in different areas of the Millungera Basin.

544 **5.4. Significance for regional tectonics**

545 Northeast Australia lies on a cratonic margin that has had a complex crustal history
546 involving the successive development of several Proterozoic to Paleozoic orogenic systems
547 (Fig. 10). Age data from the faults defining the margins of the Millungera Basin is thus
548 important in revealing concealed major Proterozoic tectonic zones in Australia, which contain
549 energy and mineral resources (Korsch et al., 2011).

550 The fault gouge ages clustering at ($\sim 1115 \pm 26$ Ma, $\sim 1070 \pm 25$ Ma, $\sim 1040 \pm 24$ Ma,
551 $\sim 1000 \pm 23$ Ma, and $\sim 905 \pm 21$ Ma (Fig. 7) may be related to the regional extension and



552 associated major thermal event that occurred across Australia at 1120-900 Ma (e.g.,
553 Musgrave Orogeny and subsequent Giles Event), due to interactions between Australia and
554 other continents during assembly of the supercontinent Rodinia (De Vries et al., 2008; Li et
555 al., 2008; Evins et al., 2010). This Australia-wide tectono-thermal event that largely
556 developed along former (Mesoproterozoic) collision zones led to emplacement of widespread
557 dyke swarms, sills and associated granite plutons in the central and north Australia craton
558 largely in a time frame between ~1040 Ma and ~1090 Ma (Schmidt et al., 2006; Evins et al.,
559 2010; Aitken et al., 2013). The Musgrave Orogeny involving widespread emplacement of
560 granite and mafic-ultramafic bodies were recorded in central Australia at 1220 Ma and 1120
561 Ma (Evins et al., 2010; Kirkland et al., 2013). Major swarms of dolerite intrusions in the
562 North Australian Craton dated at 1116 ± 12 Ma (Lakeview Dolerite, Tanaka and Idnurm,
563 1994) and associated hydrothermal events were recorded in the Mt. Isa Province (adjacent to
564 the study area, Fig. 1) (Uysal et al., 2004). The illite ages clustering around ~1100 Ma
565 coincide with the latest stage of the Musgrave Orogeny Fig. 7b, Fig. 10).

566 Another cycle of mafic intrusions in central Australia occurred during the extensional
567 Giles Event between ~1078 Ma and 1068 Ma (Evins et al., 2010; Aitken et al., 2013 and
568 references therein), which was followed by granite magmatism and accompanied felsic
569 volcanism between ~1050 Ma and ~1040 Ma (Evins et al., 2010 and references therein). The
570 latest phase of the Giles Event is represented by the felsic Smoke Hill Volcanics yielding a
571 date of 1026 ± 26 Ma. The K–Ar ages clustering around ~1040 Ma of different illite size
572 fractions from the fault gouges and sandstones are consistent with the timing of the later stage
573 of the Giles event.

574 Orogenic events post-dating the Giles event are represented by mafic dykes and rare
575 pegmatites emplaced at about 1000 Ma (Evins et al., 2010). Further, a Rb–Sr age of 897 ± 9
576 Ma is reported for dolerite from the Stuart Dyke Swarm in the southern part of the Arunta



577 Block, Northern Territory (Black et al., 1980). The Rodinia supercontinent assembled
578 through worldwide orogenic events by 900 Ma. Stresses induced by the ca. 900 Ma event
579 probably caused reactivation of older orogens within Rodinia (Li et al., 2008). The Amadeus
580 Basin in north central Australia was initiated at ~900 Ma in the late Proterozoic by crustal
581 extension, probably in associations with mafic intrusions being correlated with the Stuart
582 Dyke Swarm (Korsch and Lindsay, 1989). Fault gouge K–Ar ages of ~900 – 950 Ma for
583 various size fractions from sample Dob-449.1 and finest fraction (<0.1 mm) from Dob-389.6
584 coincide with the timing of deformation associated with these early Neoproterozoic igneous
585 and deformation events (Fig. 7b).

586 The dated faults of the Millungera Basin may be associated regionally with a series of
587 fault systems bounding rift basins in the southern Georgina Basin. Those fault zones (e.g.,
588 Burke River Structural Belt, Pilgrim Fault Zone, Greene, 2010), which are in close proximity
589 to and run parallel to the dated faults framing the Millungera Basin, occur extensively in the
590 adjacent Mt Isa Inlier (Greene, 2010; Korsch et al., 2011). The Pilgrim Fault Zone was
591 established a Mesoproterozoic structural boundary within the Mt. Isa Inlier (Greene, 2010).
592 The southern Burke River Fault, just to the west of the Millungera Basin (Fig. 1), represents a
593 rift-bounding normal fault, were reactivated and inverted to reverse faults during the mid-
594 Paleozoic Alice Springs Orogeny (~400-350 Ma) (Greene, 2010). Similarly, samples from
595 this study were taken from thrust faults at the margin of the Milungera Basin. However, the
596 ^{40}Ar – ^{39}Ar , K–Ar, and Rb–Sr ages of the fault gouge illites have been essentially preserved
597 and no tectonic event after about 905 Ma has reset the isotopic systematics of these fault
598 gouges (Fig. 10). In conclusion, our geochronological age data constrain the timing of fault
599 activity associated with the late Mesoproterozoic and early Neoproterozoic emplacement of
600 the intrusions and crustal regional extension in central-north Australia.

601

6. CONCLUSIONS



602 A new integrated study was conducted employing radiometric age dating (Rb–Sr, ^{40}Ar – ^{39}Ar ,
603 and K–Ar) of illitic clay minerals from fault gouges and Neoproterozoic host sandstones
604 bounding the recently discovered Millungera Basin in north-central Australia. Rb–Sr
605 isochron, ^{40}Ar – ^{39}Ar total gas, and K–Ar ages are consistent indicating late Mesoproterozoic
606 and early Proterozoic episodes ($\sim 1115 \pm 26$ Ma, $\sim 1070 \pm 25$ Ma, $\sim 1040 \pm 24$ Ma, $\sim 1000 \pm 23$
607 Ma, and $\sim 905 \pm 21$ Ma) of active tectonics in north-central Australia. These faulting episodes
608 correspond to timing of regional extension and associated major thermal event that occurred
609 across Australia at 1120–900 Ma, due to interactions between Australia and other continents
610 during assembly of the supercontinent Rodinia. Sr isotope and trace element data indicate that
611 fault gouge illites precipitated from fluids that interacted with deep granitic basement
612 enriched in heat-producing elements. This study provides insight into the inscrutable time-
613 space distribution of Precambrian tectonic zones in central Australia, which are responsible
614 for the formation of a number of sedimentary basins with significant energy and mineral
615 resources. Investigating core samples with preserved isotopic signature of Proterozoic fault
616 rocks avoids the effect of surface weathering of old geological terranes.

617 **Acknowledgements**

618 Support for this research was provided by Queensland Geothermal Energy Centre of
619 Excellence (QGECE) funded by the Queensland State Government. Support by Hal Gurgenci
620 (former QGECE’s director) is particularly acknowledged. The manuscript benefited from
621 comments by Tony Allan who is greatly appreciated. Espen Torgersen and Neil Mancktelow
622 are gratefully acknowledged for their very useful and constructive comments of an earlier
623 version of the paper, which helped significantly to improve the manuscript. Michael Verrall
624 is thanked for his assistance for the SEM work. We thank Yue-xing Feng and Ai Duc Nguyen
625 for their help with analytical work and technical assistance to perform Rb–Sr and trace-
626 element analyses. We thank Turgay Demir for his assistance during sample preparation, and



627 we particularly acknowledge Chris Hall for his great help in undertaking the $^{40}\text{Ar}/^{39}\text{Ar}$
628 analysis at the University of Michigan. The Geological Survey of Queensland is particularly
629 acknowledged for providing access to core sampling.

630



631 **References**

- 632 Aitken A. R. A., Smithies R. H., M. C. Dentith, A. Joly, S. Evans and Howard H. M. (2013)
633 Magmatism-dominated intracontinental rifting in the Mesoproterozoic: The
634 Ngaanyatjarra Rift, central Australia. *Gondwana Res.*, 24, 886-901.
- 635 Árkai P. (1991) Chlorite crystallinity: an empirical approach and correlation with illite
636 crystallinity, coal rank and mineral facies as exemplified by Palaeozoic and Mesozoic
637 rocks of northeast Hungary. *J. Metamorph. Geol.* 9, 723–734.
- 638 Babaahmadi, A., Uysal, I.T., Rosenbaum, G. (2019). Late Jurassic intraplate faulting in
639 eastern Australia: a link to subduction in eastern Gondwana and plate tectonic
640 reorganisation. *Gondwana Research*, 66, 1-12.
- 641 Berthé D., Choukroune P. and Jégouzo, P. (1979) Orthogneiss, mylonite and non coaxial
642 deformation of granites: the example of the South Armorican Shear Zone. *J. Struct.*
643 *Geol.* 1, 31-42.
- 644 Black L.P., Shaw R.D. and Offe, L.A. (1980) The age of the Stuart Dyke Swarm and its
645 bearing on the onset of late Precambrian sedimentation in central Australia. *J. Soc.*
646 *Austr.*, 27, 151-155.
- 647 Boles A., van der Pluijm B., Mulch A., Mutlu H., Uysal I.T. and Warr, L. (2015) Hydrogen
648 and $^{40}\text{Ar}/^{39}\text{Ar}$ isotope evidence for multiple and protracted paleofluid flow events
649 within the long-lived North Anatolian Keirogen (Turkey). *Geochem. Geophys. Geosy.*
650 16, 1975-1987.
- 651 Bröcker, M., Baldwin, S., Arkudas, R. (2013). The geological significance of $^{40}\text{Ar}/^{39}\text{Ar}$ and
652 Rb–Sr white mica ages from Syros and Sifnos, Greece: a record of continuous
653 (re)crystallization during exhumation? *J. Metamorph. Geol.* 31, 629–646.



- 654 Chester F.M., Friedman M. and Logan, J.M. (1985) Foliated cataclasites. *Tectonophysics*
655 **111**, 139-146.
- 656 Clauer N., Chaudhuri S. Kralik S. and Bonnotcourtois C. (1993) Effects of experimental
657 leaching on Rb-Sr and K-Ar isotopic systems and REE contents of diagenetic illite,
658 *Chem. Geol.* **103**, 1-16.
- 659 Clauer N., Zwingmann H., Liewig N. and Wendling R. (2012) Comparative ⁴⁰Ar/³⁹Ar and
660 K-Ar dating of illite-type clay minerals: a tentative explanation for age identities and
661 differences. *Earth-Sci. Rev.* 115, 76–96.
- 662 Clauer, N. and Liewig, N. (2013) Episodic and simultaneous illitization in oil-bearing Brent
663 Group and Fulmar Formation sandstones from the northern and southern North Sea
664 based on illite K–Ar dating. *Am. Assoc. Pet. Geol. Bull.* **97**, 2149–2171.
- 665 Craw, D., Upton, P. and Mackenzie, D.J. (2009). Hydrothermal alteration styles in ancient
666 and modern orogenic gold deposits, New Zealand. *New Zealand Journal of Geology*
667 *and Geophysics*, **52**, 11-26.
- 668 Dalrymple G.B. and Lanphere, M.A. (1969) Potassium-argon dating. W.H. Freeman, San
669 Francisco, 258 p.
- 670 Davidson, J., Charlier, B., M.H., Perlroth, R. (2005). Mineral isochrons and isotopic
671 fingerprinting: Pitfalls and promises. *Geology*, **33**, 29–32.
- 672 de Vries S.T., Pryer L.L. and Fry N. (2008) Evolution of Neoproterozoic and Proterozoic basins
673 of Australia. *Precamb. Res.*, **166**, 39–53.
- 674 Delle Piane C., Clennell M.B., Keller J.V., Giwelli A. and Luzin, V. (2017) Carbonate hosted
675 fault rocks: A review of structural and microstructural characteristic with implications
676 for seismicity in the upper crust. *J. Struct. Geol.* **103**, 17-36.



- 677 Di Vincenzo G, Tonarini S, Lombardo B, Castelli D and Ottolini L. (2006) Comparison of
678 $^{40}\text{Ar}/^{39}\text{Ar}$ and Rb-Sr data on phengites from the UHP Brossasco-Isasca unit (Dora
679 Maira Massif, Italy): implications for dating white Mica. *J. Petrol.* **47**, 1439–1465.
- 680 Duvall A.R., Clark M.K., van der Pluijm B.A. and Li C. (2011) Direct dating of Eocene
681 reverse faulting in northeastern Tibet using Ar-dating of fault clays and low-
682 temperature thermochronometry. *Earth Planet. Sci. Lett.* **304**, 520-526.
- 683 Eberl, D.D., Środoń, J., Kralik, M., Taylor, B.E, and Peterman, Z.E., 1990. Ostwald ripening
684 of clays and metamorphic minerals, *Science* 248, 474–477.
- 685 Eggins S.M., Woodhead J.D., Kinsley L.P.J., Mortimer G.E., Sylvester P., McCulloch M.T.,
686 Hergt J.M. and Handler M.R. (1997) A simple method for the precise determination
687 of ≥ 40 trace elements in geological samples by ICPMS using enriched isotope
688 internal standardization. *Chem. Geol.* **134**, 311-326.
- 689 Eichhubl, P., Davatzes, N.C., and Becker, S.P. (2010). Structural and diagenetic control of
690 fluid migration and cementation along the Moab fault, Utah. *AAPG Bulletin*, 93, 653-
691 681.
- 692 Elminen T., Zwingman, H. and Kaakinen A. (2018) Timing of brittle deformation and
693 sedimentation within the Savio tunnel site, Southern Finland – Implication for
694 sediment sources in Fennoscandia. – *Precambrian Research*, 304, 110-124,
695 doi.org/10.1016/j.precamres.2017.10.014
- 696 Evins P.M., Smithies R.H., Howard H.M., Kirkland C.L., Wingate M.T.D. and Bodorkos S.
697 (2010) Redefining the Giles Event within the setting of the 1120–1020 Ma
698 Ngaanyatjarra Rift, west Musgrave Province, Central Australia. *Geological Survey of*
699 *Western Australia, Record* 2010/6, 36p.



- 700 Faulkner, D. R., Jackson, C. A. L., Lunn, R. J., Schlische, R. W., Shipton, Z. K., Wibberley,
701 C. A. J., and Withjack, M. O. (2010). A review of recent developments concerning the
702 structure, mechanics and fluid flow properties of fault zones. *Journal of Structural*
703 *Geology* 32, 1557–1575.
- 704 Faulkner S.P., Maxwell M., O’connor L.K., Sargent S.N., and Talebi B. (2012) Coastal
705 Geothermal Energy Initiative GSQ Julia Creek 1: well completion report and heat
706 flow modelling results. *Queensland Geological Record* 2012/05.
- 707 Fedo, C.M., Nesbitt, H.W., Young and G.M. (1995). Unraveling the effects of potassium
708 metasomatism in sedimentary rocks and paleosols, with implications for
709 paleoweathering conditions and provenance. *Geology*, **23**, 21–924.
- 710 Ferry, J.M. and Dipple, G.M. (1991). Fluid flow, mineral reactions, and metasomatism.
711 *Geology*, **19**, 211-214.
- 712 Fitzell M.J., Maxwell M., O’connor L.K., Sargent S.N. and Talebi B. (2012) Coastal
713 Geothermal Energy Initiative, GSQ Dobbryn 2 Well completion report and heat flow
714 modelling results. *Queensland Geological Record* 2012/04.
- 715 Grathoff G.H. and Moore D.M. (1996) Illite polytype quantification using Wildfire[®]
716 calculated X-ray diffraction patterns. *Clay. Clay Miner.* (44) 835–842.
- 717 Greene, D.C. (2010) Neoproterozoic rifting in the southern Georgina Basin, central Australia:
718 Implications for reconstructing Australia in Rodinia. *Tectonics* **29**, TC5010,
719 doi:10.1029/2009TC002543.
- 720 Hall C. M. (2014) Direct measurement of recoil effects on ³⁹Ar-⁴⁰Ar standards. *Geol. Soc.*
721 *London Spec. Publ.*, **378**, 53-62.



- 722 Hall C. M., Higuera P. L., Kesler S. E., Lunar R., Dong H. and Halliday A. N. (1997) Dating
723 of alteration episodes related to mercury mineralisation in the Almadén district,
724 Spain. *Earth Planet. Sci. Lett.* **148**, 287–298.
- 725 Hess, J.C and Lippolt, H.J. (1994). Compilation of K-Ar measurements on HD-B1 standard
726 biotite. in : Odin G.S. (1994) : Phanerozoic time scale, Bull. Lias. Inform., IUGS
727 subcom. Geochronol., 12, Paris p. 19-23.
- 728 Hetzel, R., Zwingmann, H., Mulch, A., Gessner, K., Akal, C., Hampel, A., Güngör, T.,
729 Petschick, R., Mikes, T. and Wedin, F. (2013) Spatiotemporal evolution of brittle
730 normal faulting and fluid infiltration in detachment fault systems: a case study from
731 the Menderes Massif, western Turkey. *Tectonics* 32, 1–13.
- 732 Işık V. and Uysal I.T., Caglayan A. and Seyitoglu G. (2014) The evolution of intra-plate fault
733 systems in central Turkey: structural evidence and Ar–Ar and Rb–Sr age constraints
734 for the Savcili Fault Zone. *Tectonics* **33**, 1875–1899.
- 735 Ji J. and Browne P.R.L. (2000) Relationship between illite crystallinity and temperature in
736 active geothermal systems of New Zealand: Clay. *Clay Miner.* **48**, 139–144.
- 737 Kelley S. (2002) Excess argon in K–Ar and Ar–Ar geochronology. *Chem. Geol.* **188**, 1 – 22
- 738 Kirkland, C.L., Smithies, R.H., Woodhouse, A.J., Howard, H.M., Wingate, M.T.D.,
739 Belousova, E.A., Cliff, J.B., Murphy, R.C., Spaggiari, C.V. (2013). Constraints and
740 deception in the isotopic record; the crustal evolution of the west Musgrave
741 Province, central Australia. *Gondwana Research*, **23**, 759–781.
- 742 Korsch R.J., Lindsay, J.F. (1989). Relationships between deformation and basin evolution in
743 the intracratonic Amadeus Basin, central Australia. *Tectonophysics*, **158**, 5-22.
- 744 Korsch R.J., Struckmeyer H.I.M. Kirkby L.J., Hutton L.J., Carr L.K., Hoffmann K.,
745 Chopping R., Roy I.G., Fitzell M., Totterdell J.M., Nicoll M.G. and Talabi B. (2011)



- 746 Energy potential of the Millungera Basin: a newly discovered basin in north
747 Queensland. *The APPEA Journal* **51**, 295-332.
- 748 Korsch R. J., Huston D. L., Henderson R. A., Blewett R. S., Withnall I. W., Fergusson C. L.,
749 Collins W. J., Saygin E., Kositsin N., Meixner A. J., Chopping R., Henson P. A.,
750 Champion D. C., Hutton L. J., Wormald R., Holzschuh J. and Costelloe R. D.
751 (2012) Crustal architecture and geodynamics of North Queensland, Australia:
752 insights from deep seismic reflection profiling. *Tectonophysics* **572-573**, 76-99.
- 753 Laurich B., Urai J.L., Desbois G., Vollmer C. and Nussbaum C. (2014). Microstructural
754 evolution of an incipient fault zone in Opalinus Clay: Insights from an optical and
755 electron microscopic study of ion-beam polished samples from the Main Fault in the
756 Mt-Terri Underground Research Laboratory. *J. Struct. Geol.* **67**, 107-128.
- 757 Li H.-C., Ku T.-L., You C.-F., Cheng H., Lawrance Edwards R., Ma Z.-B., Tsai A.-S. and Li
758 M.-D. (2005) $^{87}\text{Sr}/^{86}\text{Sr}$ and Sr/Ca in speleothems for paleoclimate reconstruction
759 in Central China between 70 and 280 kyr ago. *Geochim. Cosmochim. Acta* **69**,
760 3933–3947.
- 761 Li Z. X.; Bogdanova S. V., Collins A. S., Davidson A., De Waele B., Ernst R. E., Fitzsimons
762 I. C. W., Fuck R. A., Gladkochub D. P., Jacobs J., Karlstrom K. E., Lul S., Natapov
763 L. M., Pease V., Pisarevsky S. A., Thrane K., Vernikovsky V. (2008) Assembly,
764 configuration, and break-up history of Rodinia: A synthesis. *Precamb. Res.*
765 **160**,179–210.
- 766 Lin A. (1999) S–C cataclasite in granitic rock. *Tectonophysics* **304**, 257-273.
- 767 Lonker S.W. and Gerald J.D.F. (1990) Formation of coexisting 1M and 2M polytypes in illite
768 from an active hydrothermal system. *Amer. Miner.* **75**, 1282-1289.



- 769 Ludwig K.R. (2012) User's Manual for Isoplot/Ex: a Geochronological Toolkit for Microsoft
770 Excel, 70pp.
- 771 Lupi, M., S. Geiger, and C. M. Graham (2010), Hydrothermal fluid flow within a tectonically
772 active rift-ridge transform junction: Tjörnes Fracture Zone, Iceland, *J. Geophys.*
773 *Res.*, **115**, B05104, doi:10.1029/2009JB006640.
- 774 Mancktelow N., Zwingmann H., Campani M., Fugenschuh B., Mulch A. (2015) Timing and
775 conditions of brittle faulting on the Silltal-Brenner Fault Zone, Eastern Alps
776 (Austria). *Swiss J Geosci* **108**, 305–326. Mancktelow, N., Zwingmann, H. and
777 Mulch, A. (2016) Dating of fault gouge from the Naxos detachment (Cyclades,
778 Greece). *Tectonics* 35 (10), 2334–2344.
- 779 McDougall, I., Roksandic, Z. (1974). Total fusion $^{40}\text{Ar}/^{39}\text{Ar}$ ages using HIFAR reactor.
780 *Journal of the Geological Society of Australia*, 21, 81-89.
- 781 Merriman R. J. and Frey M. (1999) Patterns of very low-grade metamorphism in metapelitic
782 rocks. In *Low Grade Metamorphism* (eds. M. Frey and D. Robinson). Blackwell
783 Science, Cambridge. pp. 61–107.
- 784 Merriman R. J. and Peacor D.R. (1999) Very low-grade metapelites: mineralogy,
785 microfabrics and measuring reaction progress. In *Low Grade Metamorphism* (eds.
786 M. Frey and D. Robinson). Blackwell Science, Cambridge. pp. 10–60.
- 787 Michalski, J.R., Reynolds, S.J., Niles, P.B., Sharp, T.G. and Christensen, P.R. (2007).
788 Alteration mineralogy in detachment zones: Insights from Swansea, Arizona.
789 *Geosphere*, 3, 84–198.
- 790 Middleton A.W., Uysal I.T., Bryan S.E., Hall C.M. and Golding S.D (2014) Integrating ^{40}Ar –
791 ^{39}Ar , ^{87}Rb – ^{87}Sr and ^{147}Sm – ^{143}Nd geochronology of authigenic illite to evaluate



- 792 tectonic reactivation in an intraplate setting, central Australia. *Geochim.*
793 *Cosmochim. Acta.* **134**, 155-174.
- 794 Mutlu H., Uysal I. T., Altunel, E., Karabacak V., Feng Y., Zhao J.-x. and Atalay O. (2010)
795 Rb–Sr systematics of fault gouges from the North Anatolian Fault Zone (Turkey), J.
796 Struct. Geol. **32**, 216-221.
- 797 Neumann, N.L. and Kositcin, N. (2011). New SHRIMP U–Pb zircon ages from north
798 Queensland, 2007–2010. *Geoscience Australia, Record*, **2011/38**, 82 p.
- 799 Nicchio M.A., Nogueira F.C., Balsamo F., Souza J.A., Carvalho B.R. and Bezerra F.H.
800 (2018) Development of cataclastic foliation in deformation bands in feldspar-rich
801 conglomerates of the Rio do Peixe Basin, NE Brazil. *J. Struct. Geol.* **107**, 132-141.
- 802 Odin G.S. and 35 collaborators (1982). Interlaboratory standards for dating purposes. in:
803 Odin, G.S. (editor) Numerical Dating in Stratigraphy. Part 1. John Wiley & Sons,
804 Chichester, 123-148.
- 805 Ohr M., Halliday A.N. and Peacor D.R. (1994) Mobility and fractionation of rare earth
806 elements in argillaceous sediments: Implications for dating diagenesis and low-
807 grade metamorphism. *Geochim. Cosmochim. Acta.* **58**, 289-312.
- 808 Parry, W. T., Hedderly-Smith, D., And Bruhn, R. L. (1991), Fluid Inclusions and
809 Hydrothermal Alteration on the Dixie Valley Fault, Nevada. *J. Geophys. Res.*, **96**,
810 19,733-19,748.
- 811 Rosenbaum G., Uysal I.T. and Babaahmadi A. (2015) The Red Rock Fault Zone (northeast
812 New South Wales): Kinematics, timing of deformation and relationships to the New
813 England oroclines. *Aust. J. Earth. Sci.* **62**, 409-423.
- 814 Rowe C.D., Kirkpatrick J.D. and Brodsky E.E. (2012) Fault rock injections record paleo-
815 earthquakes. *Earth Planet. Sci. Lett.* **335**, 154-166.



- 816 Rutter E.H., Maddock R.H., Hall S.H. and White S.H. (1986) Comparative microstructures of
817 natural and experimentally produced clay-bearing fault gouges. *Pure Appl.*
818 *Geophys.* **124**, 3-30.
- 819 Schmid S. M. and M. R. Handy (1991) Towards a genetic classification of fault rocks:
820 Geological usage and tectonophysical implications. In *Controversies in Modern*
821 *Geology: Evolution of Geological Theories in Sedimentology, Earth History and*
822 *Tectonics* (eds. D. W. Mueller, J. A. McKenzie and H. Weissert). Academic, San
823 Diego, Calif. pp. 339–361.
- 824 Schmidt P.W., Williams G.E., Camacho A. and Lee, J.K.W. (2006) Assembly of Proterozoic
825 Australia: implications of a revised pole for the ~1070 Ma Alcurra Dyke Swarm,
826 central Australia. *Geophys. J. Int.* **167**, 626–634.
- 827 Sharp Z. D. (1990) A laser-based microanalytical method for the in situ determination of
828 oxygen isotope ratios of silicates and oxides: *Geochim. Cosmochim. Acta.* **54**, 1353-
829 1357.
- 830 Sibson R. H. (1977) Fault rocks and fault mechanisms. *J. Geol. Soc. Lond.* **133**, 191–213.
- 831 Sibson R. H. (1987) Earthquake rupturing as a hydrothermal mineralising agent. *Geology* **15**,
832 701-704.
- 833 Sibson R.H. (1989) Earthquake faulting as a structural process. *Journal of Structural Geology*
834 **11**, 1-14.
- 835 Solum J.G. van der Pluijm, B.A. and Peacor D.R. (2005) Neocrystallization, fabrics and age
836 of clay minerals from an exposure of the Moab Fault, Utah. *J. Struct. Geol.* **27**,
837 1563-1576.
- 838 Srodon J. and Eberl, D.D. 1984. Illite. In *Micas*. (ed. S.W. Bailey). *Reviews in mineralogy*
839 **13**, Mineralogical Society of America. pp. 495-544.



- 840 Steiger R.H. and Jäger E. (1977) Subcommittee on geochronology: convention on the use
841 of decay constants in geochronology and cosmochronology. *Earth. Planet. Sci. Lett.*
842 **36**, 359–362.
- 843 Tanaka H. and Idnurm. M (1994). Palaeomagnetism of Proterozoic mafic intrusions and host
844 rocks of the Mount Isa Inlier, Australia: revisited. *Precamb. Res.* **69**, 241-258.
- 845 Taylor S.R. and McLennan S.M. (1985) *The Continental Crust: Its Composition and*
846 *Evolution*. Blackwell, 312.
- 847 Taylor H. P. (1997) Oxygen and hydrogen isotope relationships in hydrothermal mineral
848 deposits. In *Geochemistry of hydrothermal ore deposits*. (ed. H. L. Barnes). John
849 Wiley, New York. pp. 229–288.
- 850 Torgersen E., Viola G., Zwingmann H. and Harris C. (2014) Structural and temporal
851 evolution of a reactivated brittle-ductile fault—Part II: timing of fault initiation and
852 reactivation by K-Ar dating of synkinematic illite/muscovite. *Earth. Planet. Sci.*
853 *Lett.* **407**, 221–233
- 854 Ujiie K., Yamaguchi A., Kimura G. and Toh, S. (2007) Fluidization of granular material in a
855 subduction thrust at seismogenic depths. *Earth. Planet. Sci. Lett.*, **259**, 307-318.
- 856 Uysal I.T. and Golding S.D. (2003) Rare earth element fractionation in authigenic illite-
857 smectite from Late Permian clastic rocks, Bowen Basin, Australia: implications for
858 physico-chemical environments of fluids during illitization. *Chem. Geol.* **193**, 167-
859 179.
- 860 Uysal I.T., Glikson M., Golding S.D. and Southgate P.N. (2004) Hydrothermal control on
861 organic matter alteration and illite precipitation, Mt Isa Basin, Australia. *Geofluids*
862 **4**, 131-142.
- 863 Uysal I.T., Mory A.Y., Golding S.D., Bolhar R. and Collerson K.D. (2005). Clay
864 mineralogical, geochemical and isotopic tracing of the evolution of the Woodleigh
865 impact structure, Southern Carnarvon Basin, Western Australia. *Contrib. Mineral.*
866 *Petrol.* **149**, 576-590.
- 867 Uysal I. T., Mutlu M, Altunel A., Karabacak V. and Golding S. D. (2006) Clay mineralogical
868 and isotopic (K–Ar, $\delta\text{O-18}$, δD) constraints on the evolution of the North Anatolian
869 fault zone, Turkey. *Earth. Planet. Sci. Lett.* **243**, 181–194.



- 870 Uysal I.T., Golding S.D, Bolhar R., Zhao J-X., Feng Y., Greig A. and Baublys K. (2011)
871 CO₂ degassing and trapping during hydrothermal cycles related to Gondwana
872 rifting in eastern Australia. *Geochim. Cosmochim. Acta.* **75**, 5444–5466.
- 873 Vance D, Ayres M, Kelley SP and Harris NBW (1998) The thermal response of a
874 metamorphic belt to extension: constraints from laser Ar data on metamorphic
875 micas. *Earth. Planet. Sci. Lett.* **162**,153-164
- 876 van der Pluijm B.A., Hall C.M., Vrolijk P.J., Pevear D.R. and Covey M.C. (2001) The dating
877 of shallow faults in the Earth's crust. *Nature* **412**: 172-175.
- 878 Verdel C., van der Pluijm, B. A. and Niemi N. (2012) Variation of illite/muscovite ⁴⁰Ar/³⁹Ar
879 spectra during progressive low-grade metamorphism: an example from the US
880 Cordillera. *Contrib. Mineral. Petr.* **164**, 521–536.
- 881 Viola G., Scheiber T., Fredin O., Zwingmann H., Margreth A., Knies J. (2016)
882 Deconvoluting complex structural histories archived in brittle fault zones. *Nat.*
883 *Commun.* **7**, 13448, 1-10.
- 884 Vrolijk P. and van der Pluijm B.A. (1999) Clay gouge. *J. Struct. Geol.* **21**, 1039-1048.
- 885 Warr L.N. and Nieto, F. (1998) Interlaboratory standardization and calibration of clay
886 mineral crystallinity and crystallite size data. *J. Metamorph. Geol.* **12**, 141–152
- 887 Warr L. N. and Mählmann R.F. (2015) Recommendations for Kübler Index standardization.
888 *Clay Miner.* **50**, 283–286.
- 889 Yamasaki S., Zwingmann H., Yamada K., Tagami T. & Umeda K. (2013) Constraining
890 timing of brittle deformation and faulting in the Toki granite, central Japan.
891 *Chemical Geology*, 351, 168–174.



- 892 Zwingmann, H. and Mancktelow, N. (2004) Timing of Alpine fault gouges. *Earth Planet. Sci.*
893 *Lett.* 223 (2–4), 415–425.
- 894 Zwingmann H., Mancktelow N., Antognini M., Lucchini R. (2010) Dating of shallow faults
895 —new constraints from the Alp Transit tunnel site (Switzerland). *Geology* **38**, 487–
896 490.
- 897



898 **Figure captions**

899 **Figure 1.** Simplified map of north-central Australia showing the interpreted subsurface
900 distribution of the Millungera Basin. The surface distribution of Cenozoic and Mesozoic
901 sediments and the locations of the Proterozoic–Ordovician Basins are also shown (modified
902 from Korsch et al., 2011).

903 **Figure 2.** Photos of sampled cores showing fault gouges investigated in this study. Foliated
904 and veined clay-rich fault gouges with light grey – green colour distinctive from adjacent
905 brown hematite-rich sandstone host rock (a-e). Fault gouge veins are characterized by an
906 ultrafine-to fine-grained matrix and angular to sub-angular fragments of host sandstone of
907 various sizes, ranging from submicron to centimetres (2b). Ultracataclastic veins are
908 common, which are observed as simple veins, complex lenses, and networks (c-d).
909 Slickenside structure is commonly seen at the sharp contact between the clay-rich fault
910 gouge layers and the host rock (f-g).

911 **Figure 3.** Thin section photomicrographs (a-b) and SEM images (c-f) illustrating fault gouge
912 illites from the Millungera Basin. (a) Illite plates (white) occur in voids within detrital quartz
913 grains and as pore-filling clay between detrital grains together with chlorite. Note green –
914 yellow chlorite shown by red arrow. (b) Alteration of detrital muscovite in illite. Note illite
915 plates at the ends of the mica filling pores. (c) SEM image of sample Dob-441. Note the large
916 detrital mica grain ($>2\ \mu\text{m}$) with diffuse-blurred and irregular edges (the white material on
917 the right-hand side), while authigenic illites occur in smaller crystals ($<2\ \mu\text{m}$) with straight
918 edges. SEM image of upper anchi- and epizone sample Dob-476.6. Note rounded smaller
919 crystals (arrows), which occur partly as a constituent of larger illite plates (dashed arrows).
920 (e-f) SEM images of samples JC-408 and JC-360.7, respectively. Note euhedral (hexagonal)
921 and anhedral crystal plates with sharp and straight edges of these JC samples, which occur in



922 smaller crystal size in comparison to the Dob samples. Smaller crystal size is consistent with
923 higher illite crystallinity values of JC samples (see Table 1).

924 **Figure 4.** Microstructures of a faulted sample from Julia Creek 1 well (depth 360 m),
925 petrographic thin section is cut parallel to the inferred shear direction. A) Whole thin section
926 image collected using an optical microscope in plane polarised light showing composite S-C
927 foliation (red dashed lines illustrate the orientation of the S plane. B) Optical microscope
928 image in cross polarised light showing phyllosilicate enriched C-planes and the oblique S-
929 foliation. C) Optical microscope image in cross polarised light showing alignment of opaque
930 insoluble minerals along the S-plane (highlighted by the red arrows) indicative of pressure
931 solution. D and E) Scanning electron microscope images of the deformed rock showing
932 corroded boundaries in detrital quartz (Qtz) highlighted by the red arrows, authigenic
933 kaolinite and illite (Kao; Ill) and detrital muscovite (Msv) aligned along the C plane.

934 **Figure 5:** Faulted sample from Dobbyn 2 well (depth 441 m). A) Hand specimen showing
935 green-beige slickenside surface with striations due to frictional movement along the surface.
936 B) Polished face of the hand specimen cut parallel to the shear direction as inferred from the
937 striation direction shown in A). C) Whole thin section image collected using an optical
938 microscope in planes polarised light. The position of the thin section with respect to the hand
939 specimen is shown by the red rectangle in B); yellow dashed line bound different
940 microstructural domains of the fault rock defined as i) foliated cataclasite and ii) cataclasite.
941 White boxes indicate the location of the following images. D) Optical microscope image in
942 plane polarised light showing the slickenside surface (bound by the yellow dashed line) of the
943 samples being composed of iso-aligned phyllosilicates. Also shown is a hematite rich
944 injection vein. E) Scanning electron microscope image of the foliated cataclasite portion of
945 the samples and the characteristic S-C-C' texture (see text for details). White dashed line
946 highlights the orientation of the S-planes. F) Optical microscope image in plane polarised



947 light showing a slip surface (bound by the yellow dashed line) at the boundary between the
948 foliated and non-foliated cataclasite domains. G) Optical microscope image in plane polarised
949 light showing a network of hematite filled intra-crystalline micro-fractures in the cataclasite
950 domain of the fault rock, mainly composed of quartz (white grains) and pore filling clays.

951 **Figure 6.** Ar–Ar dating results and argon release diagrams for illites from the fault gouges of
952 $<2\ \mu\text{m}$ size fraction. Note consistent Ar–Ar total gas ages except for sample Dob-476.6.

953 **Figure 7.** A) Histogram for K–Ar and Ar–Ar ages and probability distribution of ages for
954 fault gouge illites. Curves show relative probabilities calculated using Isoplot 7 for Excel
955 (Ludwig, 2012). B) K–Ar and Ar–Ar dates (no error bars due to small errors) for different
956 size fractions of fault gouges and C) matrix illites from host rocks and their interpretation in
957 relation to tectonic history.

958 **Figure 8.** A) Rb–Sr data of the different size fractions and the untreated, leachate and residue
959 separates of each size fractions from sample. Parallel linear relationships correspond to
960 similar isochron age, but with different initial $^{87}\text{Sr}/^{86}\text{Sr}$ values. B) Rb–Sr plot for untreated
961 and residues of $<2\ \mu\text{m}$ fractions from most Julia Creek 1 samples. C) Well-defined isochron
962 for Julia Creek 1 samples after omitting two untreated aliquots D) Rb–Sr isochron diagrams
963 for an assemblage of Dobbyn 2 samples (including JC-360.7B $<0.5\ \mu\text{m}$) and E) another
964 group of Dobbyn 2 samples with a younger age.

965 **Figure 9.** REE patterns of the fault gouge illites. Note that the illites are substantially
966 enriched in light REE (LREE) relative to PAAS.

967 Figure 10. Summary of the geological history of the Millungera basin region and isotopic age
968 clusters of the illites.

969



Table 1. Clay mineralogy and age data of fault gouges and host rocks from Julia Creek 1 (JC) and Dobbyn 2 (Dob).

Sample & size fraction	Clay mineralogy	IC (Δ20)	ChC (Δ20)	Very-low-grade metamorphic zone	2M %	1M %	1M _d %	Rb–Sr isochron age	Ar–Ar total gas age	K–Ar age	K ₂ O (%)	⁴⁰ Ar _{rad} (%)	⁴⁰ Ar _{rad} (10 ⁻¹⁰ mol/g)
Fault gouge													
JC-321 <2mm	illite	0.59		Diagenetic									
JC-326.1 <2μm	illite	0.69		Diagenetic									
JC-343.3 <2μm	illite, kaol., chl.	0.63		Diagenetic	68	14	18			1044.0 ± 24.4	7.10	99.3	174.1
JC-343.3 0.5–0.1μm	illite, kaol., chl.	0.79		Diagenetic						1039.2 ± 24.0	6.86	99.7	167.2
JC-343.3 <0.1μm	illite	0.92		Diagenetic						1025.3 ± 23.7	6.33	99.6	151.6
JC-360.7 <2μm	illite, kaol., chl.	0.63		Diagenetic	66	18	16	1023 ± 12	1038.1 ± 2.9	1014.9 ± 23.7	7.61	99.3	179.8
JC-360.7 2–1μm	illite, kaol., chl.	0.65		Diagenetic	58	22	20			1038.9 ± 24.0	7.49	99.4	182.5
JC-360.7 <1μm	illite, kaol., chl.	0.73		Diagenetic						1041.1 ± 24.1	7.49	99.5	183.0
JC-360.7 <0.5μm	illite	0.75		Diagenetic						1005.5 ± 23.1	7.65	99.6	178.6
JC-387.8 <2μm	illite, kaol., chl.	0.57		Diagenetic									
JC-408 >2μm	illite, kaol., chl.	0.42		Upper anchizone						1243.2 ± 29.1	7.64	99.7	237.1
JC-408 2–1μm	illite, kaol., chl.	0.63		Diagenetic	63	14	23			1118.7 ± 25.9	7.94	99.6	213.4
JC-408 <2μm	illite, kaol., chl.	0.60		Diagenetic	64	17	19		1040.0 ± 2.3	1115.8 ± 26.1	7.88	99.5	211.1
JC-408 <1μm	illite, kaol., chl.	0.70		Diagenetic	64	15	22			1118.2 ± 25.9	7.81	96.6	209.8
JC-408 <0.5μm	illite	0.82		Diagenetic						1104.0 ± 25.4	7.82	99.7	206.5
JC-430.4 <2μm	illite, kaol., chl.	0.51		Lower anchizone									
JC-440.5 <2μm	illite, kaol., chl.	0.44		Lower anchizone	58	24	18	1023 ± 12		1048.9 ± 24.5	6.60	99.4	176.3
JC-440.5 0.5–0.1μm	illite, kaol., chl.	0.84		Diagenetic						1020.3 ± 23.6	7.41	99.8	168.8
JC-440.5 <0.1μm	illite	1.01		Diagenetic						1017.6 ± 23.5	7.12	99.8	168.8
JC-473-A <2μm	illite, chl.	0.51	0.35	Lower anchizone									
JC-473-B <2μm	illite, chl.	0.47		Lower anchizone									
JC-483.2 <2μm	illite, chl.	0.60	0.42	Diagenetic									
Dob-389.6 2–1μm	illite, kaol., chl.	0.42		Upper anchizone	95		5			1081.8 ± 25.0	5.97	99.7	153.5
Dob-389.6 <2μm	illite, kaol., chl.	0.43		Upper anchizone	90		10	1033 ± 25		1071.2 ± 25.0	6.53	99.7	165.7
Dob-389.6 1–0.5μm	illite, kaol., chl.	0.51		Lower anchizone	90		10			1037.8 ± 24.0	7.32	99.6	178.1
Dob-389.6 0.5–0.1μm	illite, kaol.	0.62		Diagenetic	80		20			1053.0 ± 24.3	7.20	99.7	178.6
Dob-389.6 <0.5μm	illite, kaol.	0.63		Diagenetic						981.8 ± 22.6	7.63	99.8	172.7
Dob-389.6 <0.1μm	illite, kaol.	1.00		Diagenetic						905.4 ± 20.9	6.62	99.6	135.0
Dob-417 <2μm	illite, kaol., chl.	0.50		Lower anchizone									
Dob-441 >2μm	illite, kaol., chl.	0.36		Upper anchizone						1312.3 ± 30.7	3.72	99.5	124.5
Dob-441 <2μm	illite, kaol., chl.	0.42		Upper anchizone	95		5	1033 ± 25	1068.1 ± 1.8	1148.7 ± 26.9	4.98	99.3	138.7
Dob-441 <1μm	illite, kaol., chl.	0.51		Lower anchizone	95		5			1086.5 ± 25.1	6.10	99.4	157.7
Dob-441 <0.5μm	illite, kaol., chl.	0.42		Upper anchizone						1063.3 ± 24.4	6.05		
Dob-449.1 <2μm	illite, kaol., chl.	0.29		Epizone	100			1033 ± 25		949.1 ± 22.2	6.40	99.5	138.6
Dob-449.1 2–0.5μm	illite, kaol., chl.	0.39		Upper anchizone						924.9 ± 21.4	6.63	99.8	138.9
Dob-449.1 1–0.5μm	illite, kaol., chl.	0.35		Upper anchizone						903.1 ± 20.9	6.73	99.6	136.8
Dob-449.1 <0.5μm	illite, kaol., chl.	0.37		Upper anchizone						912.6 ± 21.1	5.43	100	111.9
Dob-449.3 >2μm	kaol., illite, chl.	0.14		Epizone						1259.0 ± 29.1	0.402	100	12.70
Dob-449.3 <2μm	illite, kaol., chl.	0.19		Epizone									
Dob-449.3 2–1μm	kaol., chl., illite	0.21		Epizone						1047.7 ± 24.2	0.294	100	7.24
Dob-449.3 1–0.5μm	kaol., chl., illite	0.27		Epizone						1117.2 ± 25.8	0.554	99.4	14.87
Dob-449.3 0.5–0.2μm	kaol., chl., illite	0.25		Epizone						950.9 ± 22.0	6.02	99.7	130.7
Dob-449.3 <0.5μm	kaol., chl., illite	0.25		Epizone						1004.4 ± 23.2	0.428	99.8	9.98
Dob-476.6 >2μm	illite, kaol., chl.	0.26		Epizone						1170.4 ± 27.4	2.15	99.5	61.43
Dob-476.6 2–1μm	illite, kaol., chl.	0.29		Epizone	100					975.7 ± 22.2	4.43	99.4	101.7
Dob-476.6 <2μm	illite, kaol., chl.	0.33		Upper anchizone	100			1000 ± 12	994.6 ± 2.2	983.7 ± 23.0	4.80	99.4	108.9
Dob-476.6 <1μm	illite, kaol., chl.	0.31		Epizone	100					922.2 ± 21.2	6.18	100.0	129.0
Host whole rock													
JC-360.6 <2μm	illite	0.48		Lower anchizone									
JC-360.6 2–1μm	illite	0.68		Diagenetic						1066.9 ± 24.6	6.13	99.61	157.7
JC-360.6 1–0.5μm	illite	0.82		Diagenetic						1065.4 ± 24.6	6.90	99.7	173.8
JC-360.6 0.5–0.2μm	illite	0.52		Lower anchizone						1053.8 ± 24.3	6.68	99.2	165.8
JC-360.6 <0.2μm	illite	0.78		Diagenetic						928.3 ± 47.6	6.63	99.05	139.6
JC-490.2 <2μm	illite, chl.	0.46	0.36	Lower anchizone									
JC-500 <2μm	illite, chl.	0.51	0.36	Lower anchizone									
JC-500 2–1μm	illite, chl.	0.66		Diagenetic						1092.0 ± 25.2	3.37	99.69	87.71
JC-500 1–0.5μm	illite, chl.	0.62		Diagenetic						1076.8 ± 24.8	5.15	99.67	131.6
JC-500 0.5–0.2μm	illite, chl.	0.64		Diagenetic						1066.7 ± 24.5	5.39	99.47	135
JC-500 <0.2μm	illite, chl.	0.63		Diagenetic						878.3 ± 45.1	5.41	99.02	106.2
Dob-499.4 >2μm	illite, kaol., chl.	0.22		Epizone						1156.2 ± 26.6	0.37	97.1	10.26
Dob-499.4 <2μm	illite, kaol., chl.	0.20		Epizone									
Dob-499.4 2–1μm	illite, kaol., chl.	0.23		Epizone						1115.8 ± 25.7	2.03	99.6	54.38
Dob-499.4 1–0.5μm	illite, kaol., chl.	0.20		Epizone						1047.3 ± 24.1	5.08	99.5	43 125.1
Dob-499.4 0.5–0.2μm	illite, kaol., chl.	0.18		Epizone						1068.2 ± 24.6	3.30	99.3	83.41
Dob-499.4 <0.2μm	illite, kaol., chl.	0.21		Epizone						1025.6 ± 52.6	3.63	97.5	86.97

Calibration of the illite crystallinity (IC) and chlorite crystallinity (ChC) values and determination of very-low-grade- metamorphic zones

has been done according to Warr and Mählmann (2015) and Warr and Cox (2016). kaol. = kaolinite, chl. = chlorite.



STANDARD ID	K [%]	Rad. ⁴⁰ Ar (mol/g)	Rad. ⁴⁰ Ar (%)	Age (Ma)
HD-B1-137	7.96	3.3431E-10	89.76	24.06
LP6-151	8.37	1.9477E-09	97.28	129.4
HD-B1-139	7.96	3.4214E-10	92.33	24.63
LP6-153	8.37	1.9465E-09	97.32	129.3
HD-B1-140	7.96	3.3805E-10	92.39	24.33
LP6-154	8.37	1.9196E-09	97.39	127.6
HD-B1-141	7.96	3.4399E-10	92.86	24.76
LP6-155	8.37	1.9304E-09	97.69	128.3
HD-B1-142	7.96	3.4500E-10	93.28	24.83
LP6-156	8.37	1.9285E-09	97.59	128.1
HD-B1-147	7.96	3.4124E-10	92.88	24.56
LP6-161	8.37	1.9257E-09	97.13	127.9
HD-B1-148	7.96	3.3633E-10	90.67	24.21
LP6-162	8.37	1.9236E-09	97.21	127.8
HD-B1-149	7.96	3.3562E-10	90.93	24.16
LP6-163	8.37	1.9234E-09	97.21	127.8

Airshot ID	⁴⁰ Ar/ ³⁶ Ar	+/-
AS131-AirS-1	295.67	0.45
AS131-AirS-2	293.43	0.46
AS133-AirS-1	298.42	0.14
AS133-AirS-2	297.35	0.29
AS134-AirS-1	295.81	0.14
AS134-AirS-2	296.65	0.08
AS135-AirS-1	296.59	0.13
AS135-AirS-2	296.76	0.17
AS136-AirS-1	295.22	0.24
AS136-AirS-2	296.69	0.27
AS141-AirS-1	295.85	0.28
AS141-AirS-2	296.53	0.23
AS142-AirS-1	294.87	0.23
AS142-AirS-2	296.52	0.18
AS143-AirS-1	294.16	0.20
AS143-AirS-2	296.81	0.17

HD-B1: Hess and Lippolt (1994).

LP-6: Odin et al. (1982).

Recommended ⁴⁰Ar/³⁶Ar value: 295.5; Steiger and Jäger (1977).



Table 3. ^{87}Rb - ^{86}Sr data for the untreated (U) and acid leached residues (R) of different clay fractions from the Milungera Basin fault gouges.

Sample	Size fraction (μm)	Rb (ppm)	Sr (ppm)	$^{87}\text{Rb}/^{86}\text{Sr}$	$^{87}\text{Sr}/^{86}\text{Sr}$	$\pm 2\sigma$
JC-343.3U	<2	263.8	244.7	3.14	0.771035	0.000008
JC-360.7U	<2	270.5	303.9	2.59	0.757396	0.000009
JC-360.7R	<2	253.7	269.0	2.74	0.759576	0.000009
JC-360.7R	2-1	279	361.1	2.25	0.754344	0.000008
JC-360.7L	2-1	61.96	914.2	0.678	0.715331	0.000006
JC-360.7R	<0.5	288.7	222.1	1.30	0.778401	0.000005
JC-360.7L	<0.5	68.94	906.2	0.076	0.715632	0.000006
JC-387.8U	<2	203.7	564.6	1.05	0.734125	0.000009
JC-387.8R	<2	201.6	537.4	1.09	0.735621	0.000007
JC-408U	<2	273.0	259.4	3.06	0.768788	0.000009
JC-440.5U	<2	206.8	637.0	0.941	0.733108	0.000007
JC-440.5R	<2	213.2	627.4	0.986	0.734396	0.000009
JC-440.5R	<0.5	279.2	240.1	1.16	0.765505	0.000006
JC-440.5L	<0.5	26.75	378.4	0.071	0.716576	0.000006
Dob-389.6U	2	239.5	184.5	3.78	0.778229	0.000009
Dob-389.6R	2-1	255.0	254.5	1.00	0.769394	0.000006
Dob-389.6R	<0.5	268.6	201.0	1.34	0.783259	0.000008
Dob-389.6L	<0.5	22.08	612.8	0.04	0.712000	0.000006
Dob-441U	<2	134.8	121.6	3.23	0.770115	0.000008
Dob-441R	2-1	200.7	203.4	0.987	0.767702	0.000006
Dob-441R	<1	202.1	201.8	1.00	0.768636	0.000007
Dob-441L	<1	20.5	399.5	0.051	0.720827	0.000006
Dob-449.1U	<2	214.7	337.0	1.85	0.750186	0.000009
Dob-449.1R	<2	218.9	326.1	1.95	0.751971	0.000014
Dob-449.1R	2-1	242.0	378.8	0.639	0.749952	0.000006
Dob-449.1L	2-1	13.59	265.7	0.051	0.718102	0.000006
Dob-476.6U	<2	190.0	521.6	1.06	0.744176	0.000009
Dob-476.6R	<2	200.2	517.7	1.12	0.744209	0.000007

U= untreated, R = residue, L = leachate

972

973



Table 4. Trace element data (ppm) for the fault gouge illites.

Sample	JC-360.7	JC-387.8	JC-440.5	Dob-389.6	Dob-449.1	Dob-476.6	PAAS
La	89.8	281.5	242.3		328.0	396.2	38.0
Ce	193.9	619.1	519.4		591.8	773.3	80.0
Pr	19.9	63.1	54.3		73.1	80.2	8.90
Nd	69.1	225.6	187.3		257.0	271.5	32.0
Sm	12.8	39.1	32.2		44.5	46.3	5.60
Eu	2.22	4.32	4.22		7.30	7.01	1.10
Gd	9.27	24.3	21.2		29.8	28.7	4.70
Tb	1.05	2.07	2.59		3.70	3.23	0.77
Dy	5.09	7.22	12.9		20.2	15.9	4.40
Ho	0.94	1.17	2.42		4.36	3.29	1.00
Er	2.59	3.27	6.66		14.2	10.5	2.90
Tm	0.37	0.43	0.97		2.47	1.74	0.40
Yb	2.36	2.81	6.29		18.0	12.3	2.80
Lu	0.35	0.41	0.93		2.87	1.93	0.43
Th	80.8	110.9	83.6		107.7	149.1	14.60
U	7.54	8.43	18.6		32.2	40.3	3.10
Sc	20.7	10.2	11.2		91.4	58.1	16.00
(La/Lu) _c	29	23	76		13	29	10
Th/Sc	3.9	10.9	7.5		1.2	2.6	0.9
Th/U	10.7	13.2	4.5		3.3	3.7	4.7



Figure 1

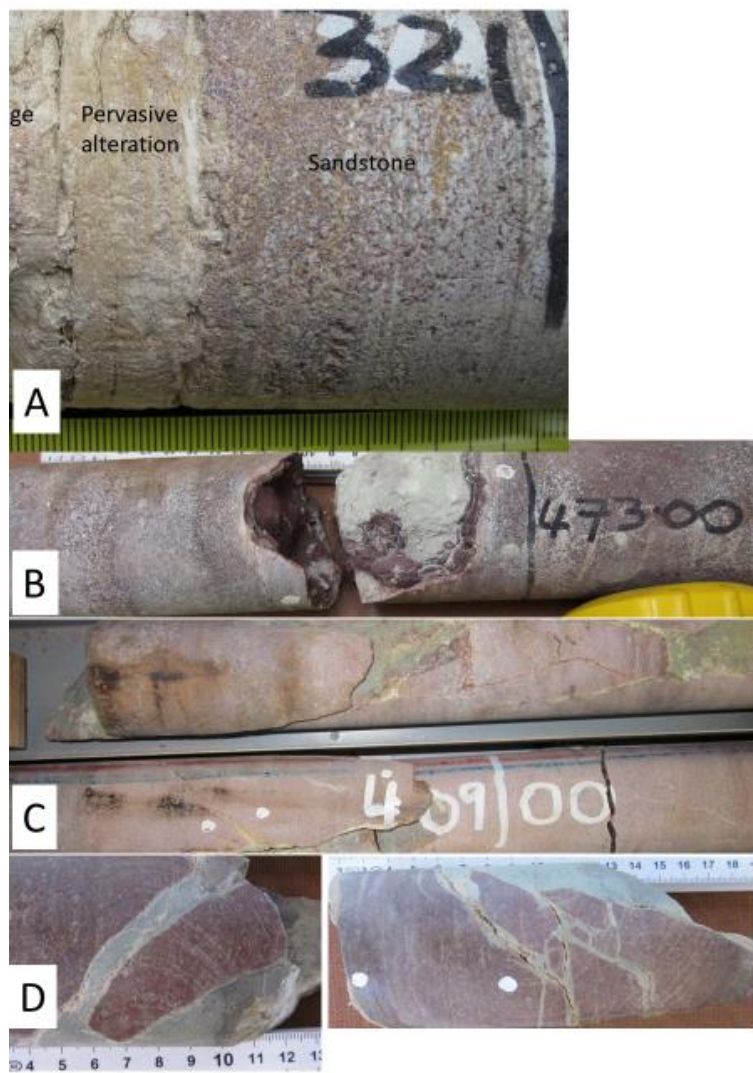




Fig. 2

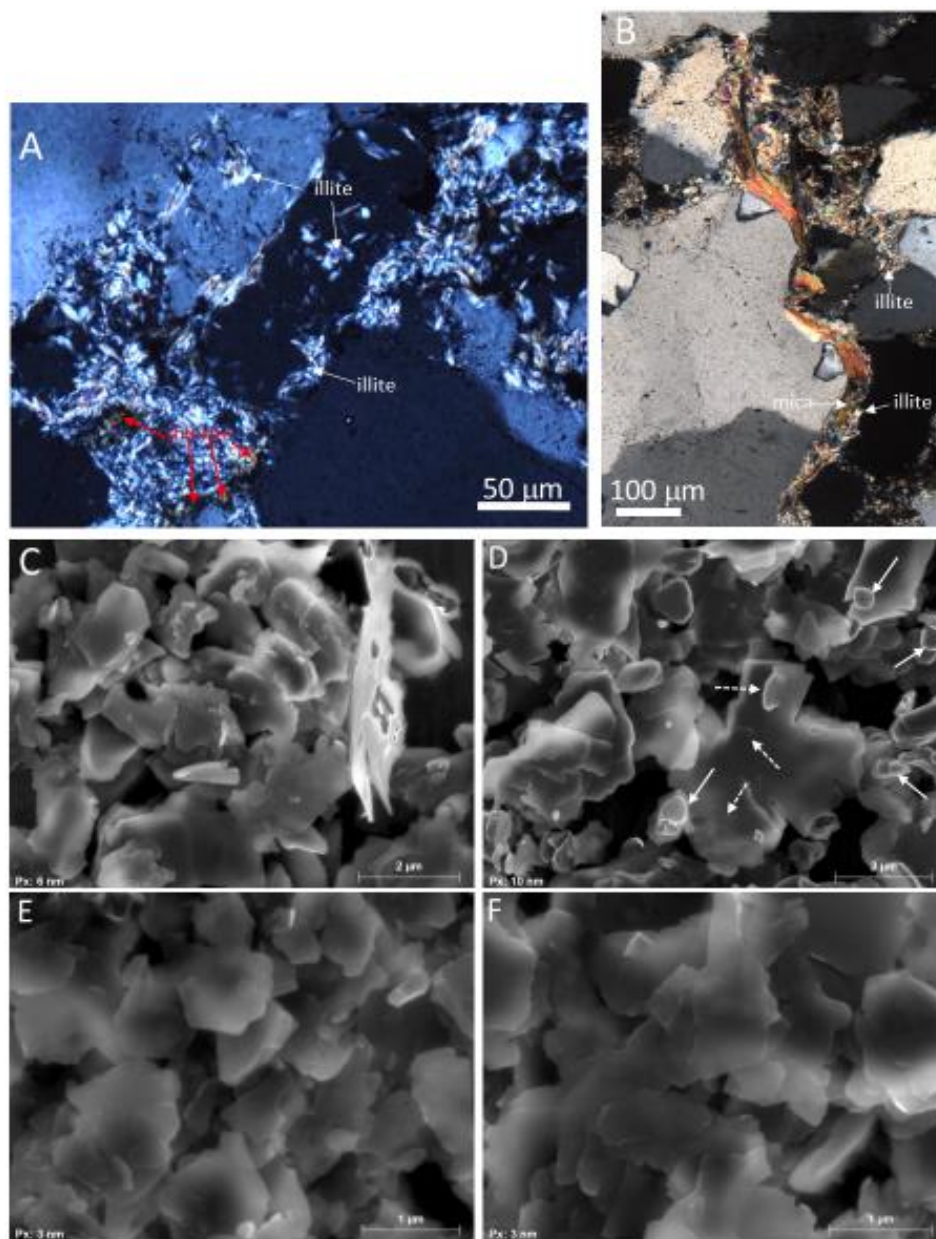
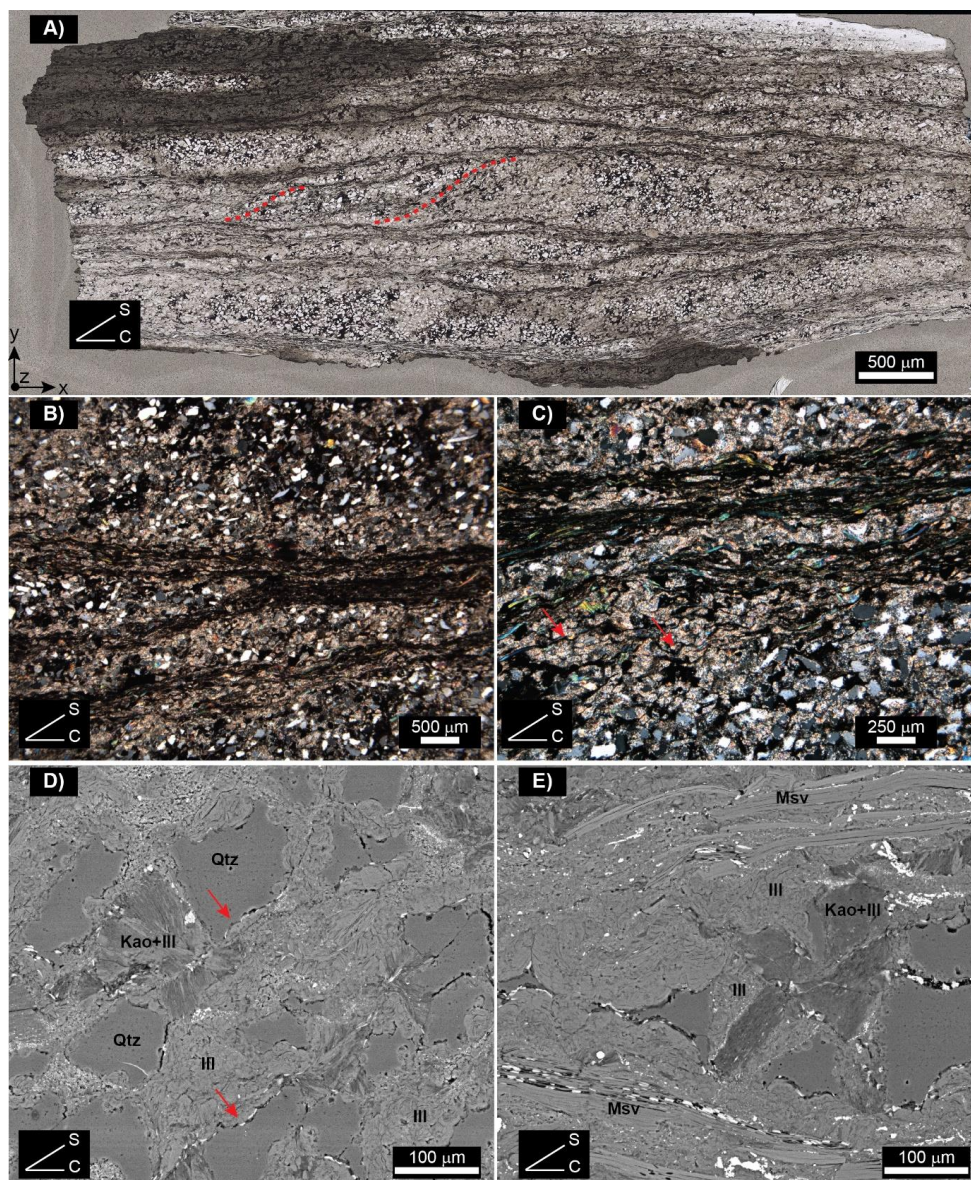
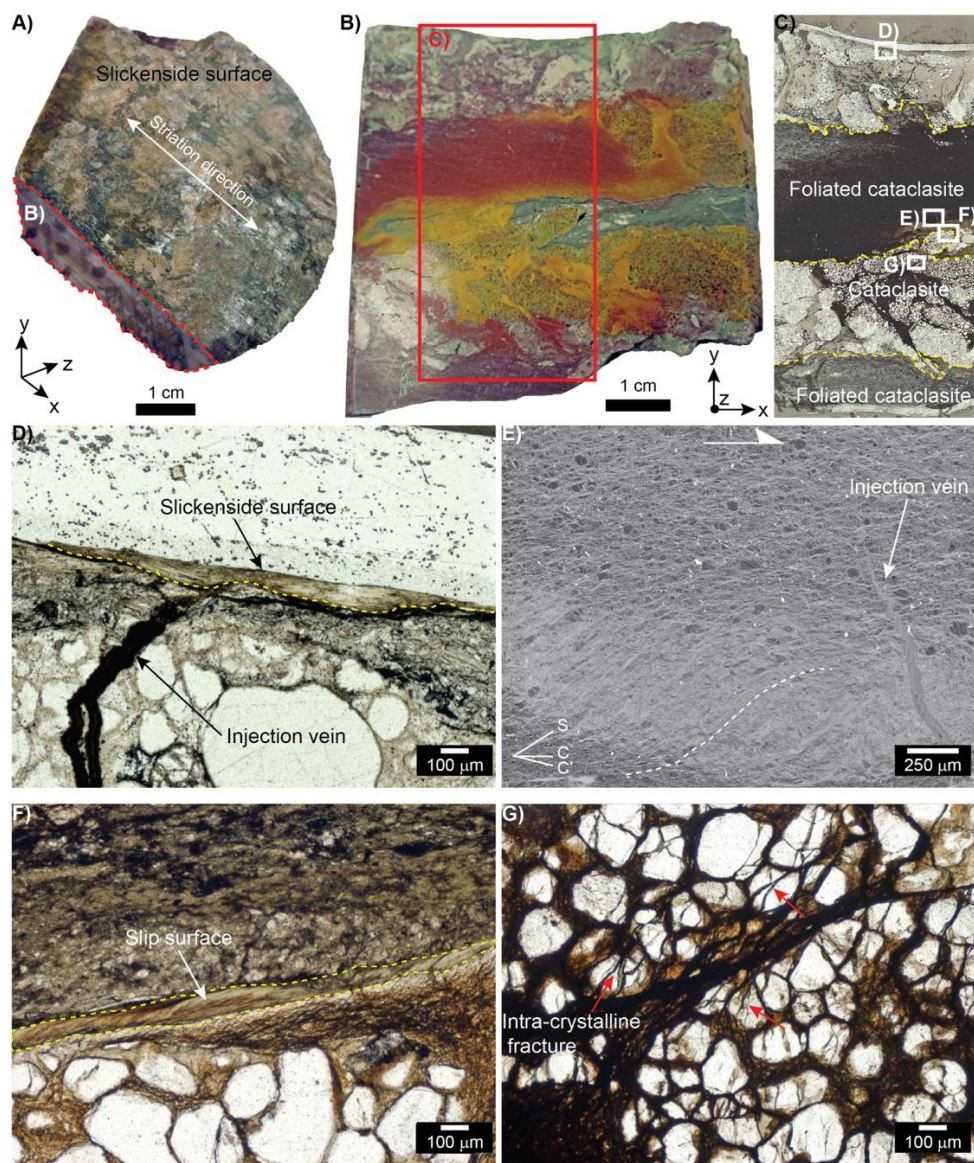


Figure 3.



1001

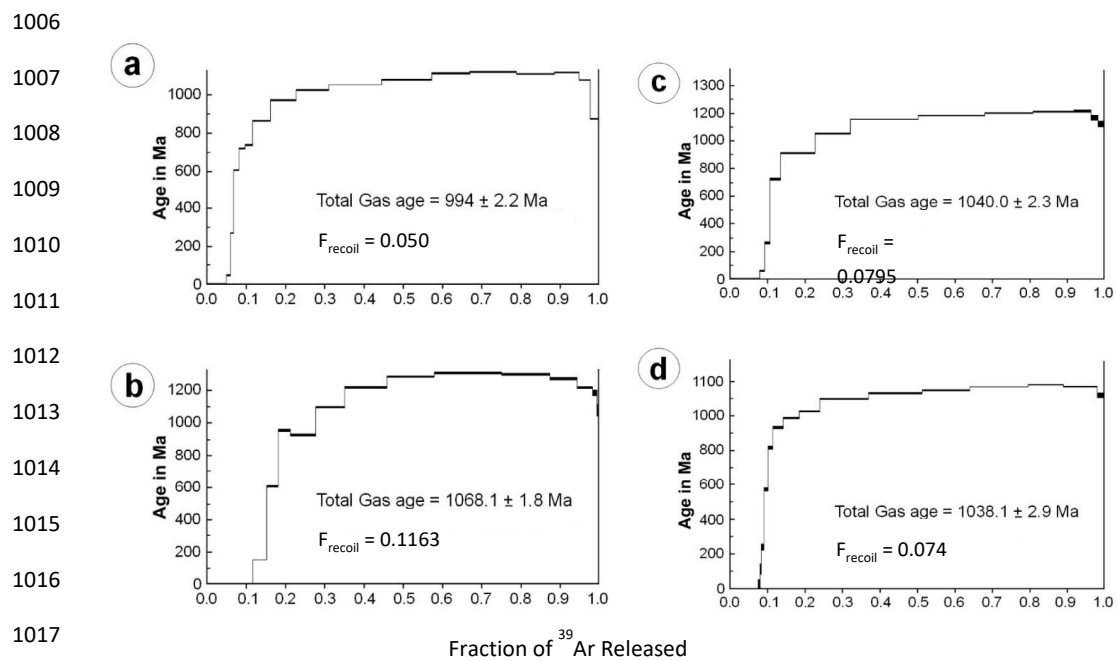
1002 Figure 4



1003

1004 Figure 5

1005



1018 Figure 6

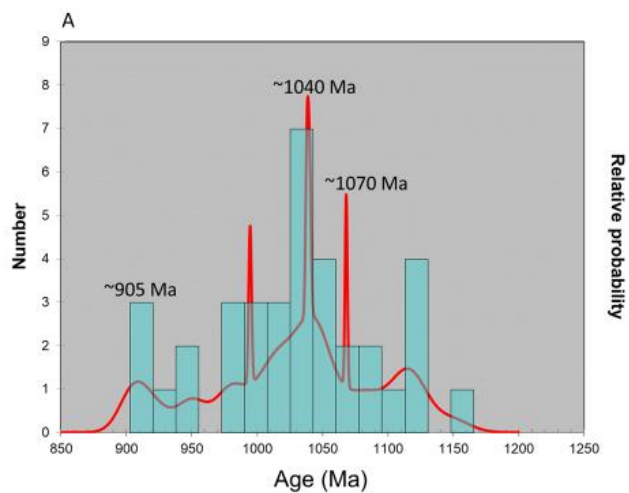


Figure 7a

1019

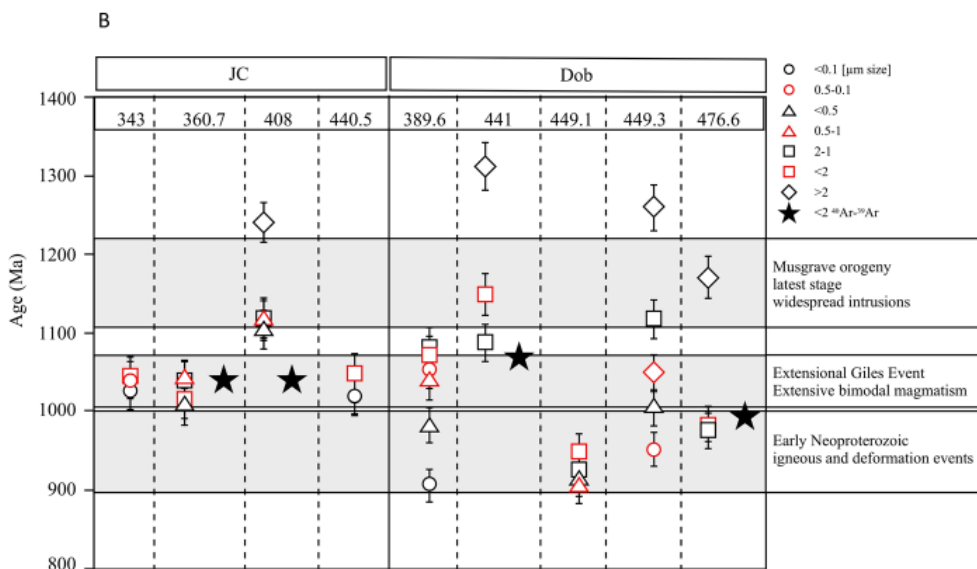


Figure 7b

1020

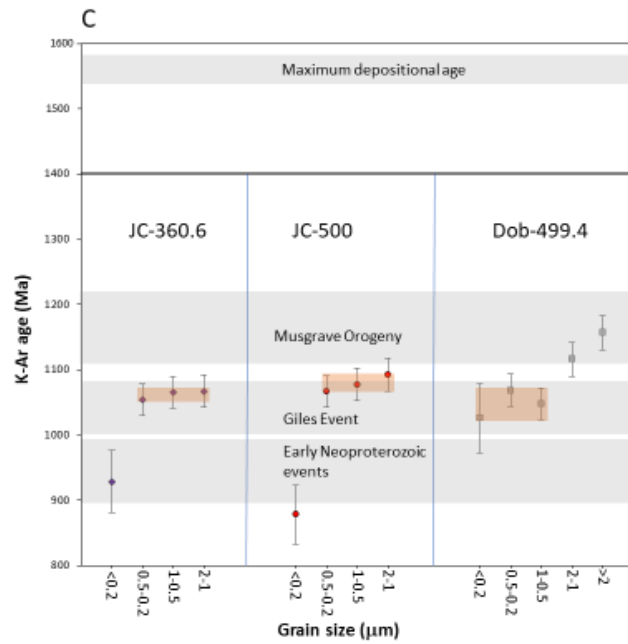


Figure 7c

1021

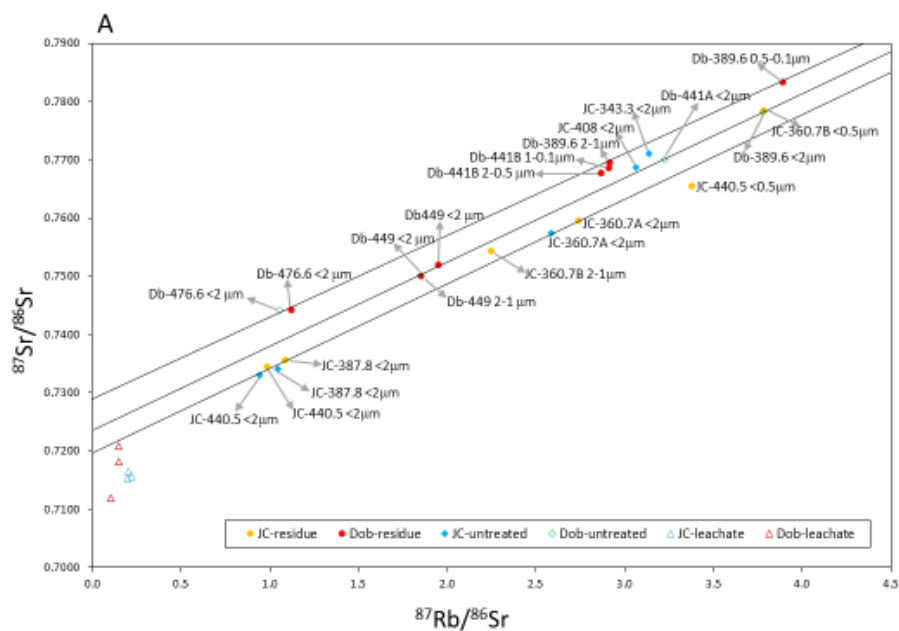


Figure 8a

1022

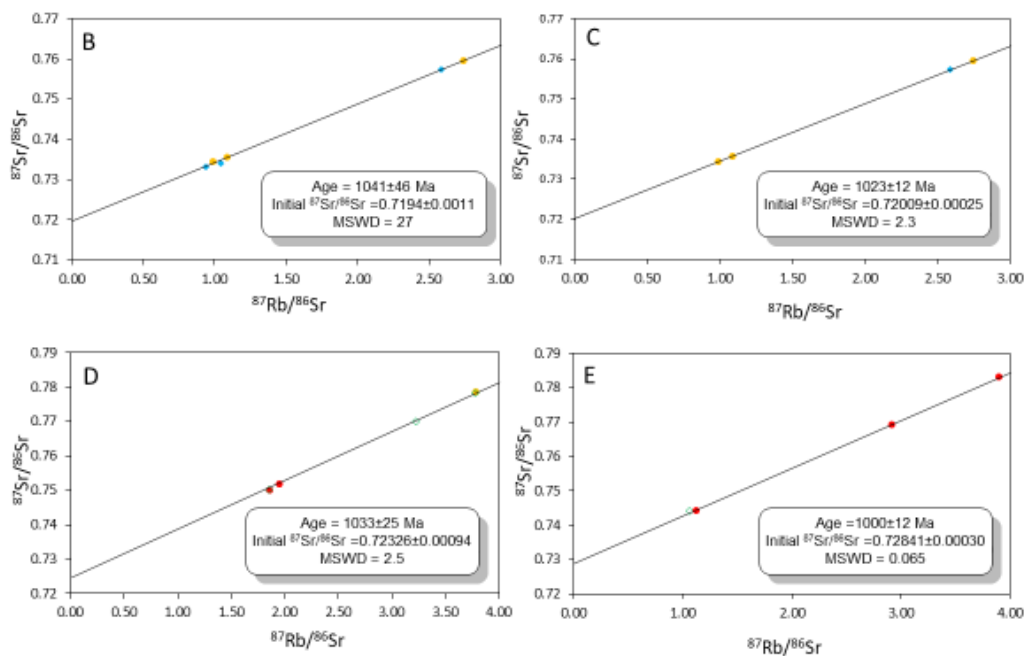
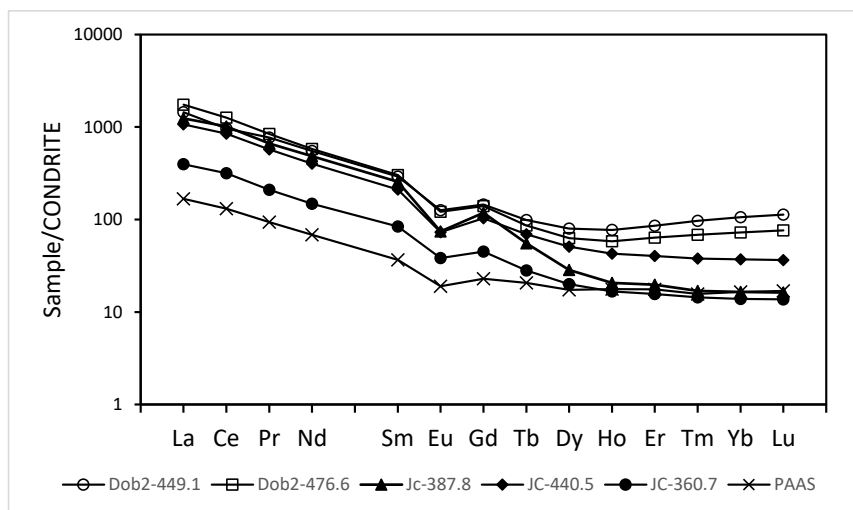


Figure 8b-e

1023

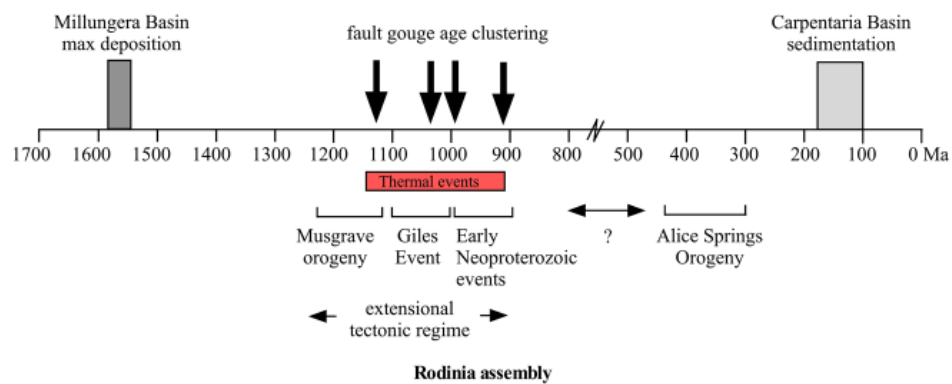
1024



1025

1026 Figure 9

1027



1028

1029 Figure 10

1030